Article

Developmental Cell

LDO proteins and Vac8 form a vacuole-lipid droplet contact site to enable starvation-induced lipophagy in yeast

Graphical abstract

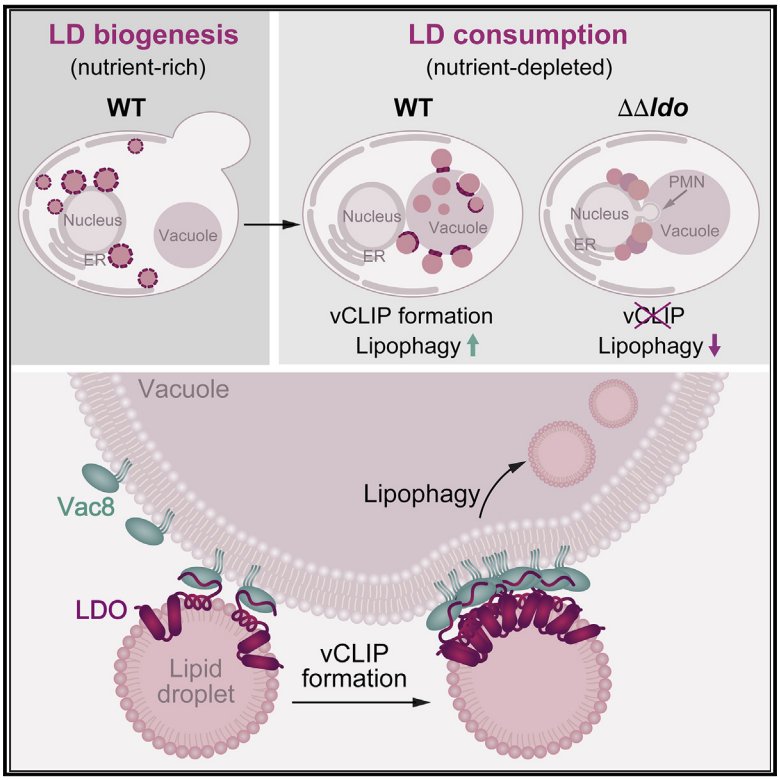

Highlights

- LDO proteins bind Vac8 to form vCLIP, the vacuole-lipid droplet contact site
- Nutrient exhaustion drives vCLIP formation to promote lipophagy
- vCLIP is critical for lipophagy and supports caloric-restriction-induced longevity
- Disruption of vCLIP induces NVJ expansion and microautophagy of the nucleus

Authors

Irene Álvarez-Guerra, Emma Block, Filomena Broeskamp, ..., Tim P. Levine, Johanna L. Höög, Sabrina Büttner

Correspondence

sabrina.buettner@su.se

In brief

Álvarez-Guerra et al. identify the tethering machinery of the membrane contact site that enables lipid droplet consumption via lipophagy. They show that nutrient exhaustion drives the formation of vCLIP, the vacuole-lipid droplet contact site established by the LDO proteins that bind vacuolar Vac8.

Álvarez-Guerra et al., 2024, Developmental Cell *59*, 1–17
March 25, 2024
https://doi.org/10.1016/j.devcel.2024.01.014

CellPress

Developmental Cell

CellPress
OPEN ACCESS

Article

LDO proteins and Vac8 form a vacuole-lipid droplet contact site to enable starvation-induced lipophagy in yeast

Irene Álvarez-Guerra,[1] Emma Block,[1] Filomena Broeskamp,[2] Sonja Gabrijelčič,[1] Terence Infant,[1] Ana de Ory,[1] Lukas Habernig,[1] Claes Andréasson,[1] Tim P. Levine,[3] Johanna L. Höög,[2] and Sabrina Büttner[1,4,*]

[1]Department of Molecular Biosciences, The Wenner-Gren Institute, Stockholm University, 10691 Stockholm, Sweden
[2]Department of Chemistry and Molecular Biology, University of Gothenburg, 40530 Gothenburg, Sweden
[3]UCL Institute of Ophthalmology, Bath Street, London EC1V 9EL, UK
[4]Lead contact
*Correspondence: sabrina.buettner@su.se
https://doi.org/10.1016/j.devcel.2024.01.014

SUMMARY

Lipid droplets (LDs) are fat storage organelles critical for energy and lipid metabolism. Upon nutrient exhaustion, cells consume LDs via gradual lipolysis or via lipophagy, the *en bloc* uptake of LDs into the vacuole. Here, we show that LDs dock to the vacuolar membrane via a contact site that is required for lipophagy in yeast. The LD-localized LDO proteins carry an intrinsically disordered region that directly binds vacuolar Vac8 to form vCLIP, the vacuolar-LD contact site. Nutrient limitation drives vCLIP formation, and its inactivation blocks lipophagy, resulting in impaired caloric restriction-induced longevity. We establish a functional link between lipophagy and microautophagy of the nucleus, both requiring Vac8 to form respective contact sites upon metabolic stress. In sum, we identify the tethering machinery of vCLIP and find that Vac8 provides a platform for multiple and competing contact sites associated with autophagy.

INTRODUCTION

Cellular adaptation to changing metabolic demands requires efficient communication between organelles and remodeling of subcellular structures. Direct physical contact between organelles at dedicated membrane contact sites provides ancient communication routes and hubs for metabolic exchange present in organisms ranging from yeast to humans.[1–3] Membrane contact sites are established by an array of tethering proteins that bridge virtually all pairs of organelles, facilitating the bidirectional exchange of biochemical information in form of metabolites, ions, and lipids.[1,2,4,5] These organelle contacts are key to intracellular signaling and are emerging as important sites for metabolic adaptation.[3,6,7]

In yeast, a contact site that dynamically changes size and architecture in response to nutrient availability is the nucleus-vacuole junction (NVJ). NVJ connects the main anabolic and catabolic compartments by establishing proximity between the nuclear endoplasmic reticulum (nER) and the vacuole, the yeast lysosome.[8–12] When nutrients are depleted, NVJs expand and coordinate distinct aspects of lipid metabolism, including the subcellular organization of lipid droplets (LDs).[11–13] LDs are dynamic fat storage organelles with critical roles in lipid and energy metabolism that allow cells to adapt to changing nutritional cues.[14,15] They consist of a neutral lipid core, particularly triacylglycerols (TAGs) and sterol esters, delimited by a phospholipid monolayer that originates from the outer leaflet of the ER membrane and contains integral and peripheral proteins.[14] Due to the absence of a bilayer, LDs cannot engage in vesicle trafficking but rely on communication via membrane contact sites.[16–21]

Depending on the metabolic status, cells alternate between LD biogenesis and LD consumption via gradual enzymatic lipolysis or via lipophagy.[22–25] Lipophagy is based on *en bloc* import into the lysosome/vacuole and plays a key role in LD consumption. In mammalian cells, uptake into the lysosome is mediated by macroautophagy, in which autophagosomes sequester LDs for delivery to the lysosome.[26,27] Notably, an alternative lipophagic route for LD consumption has recently been described in hepatocytes.[28] Here, LDs directly dock to lysosomes to be engulfed in a process that resembles microlipophagy, which is the main route of lipophagic LD consumption in yeast.[29–32] During microlipophagy, LDs redistribute around the yeast vacuole and associate with liquid-ordered (L_o) microdomains on the vacuolar membrane before being engulfed.[33,34] Though contact formation via molecules that bridge the LDs and the vacuole/lysosome is anticipated to support LD engulfment, no such molecules have been identified. Still, proximity-based approaches employing LD-localized and vacuolar resident proteins suggest the existence of such a vacuole-lipid droplet contact site (vCLIP).[20]

Here, we uncover the molecular architecture of the contact site that anchors LDs to the vacuole to facilitate lipophagy in

Please cite this article in press as: Álvarez-Guerra et al., LDO proteins and Vac8 form a vacuole-lipid droplet contact site to enable starvation-induced lipophagy in yeast, Developmental Cell (2024), https://doi.org/10.1016/j.devcel.2024.01.014

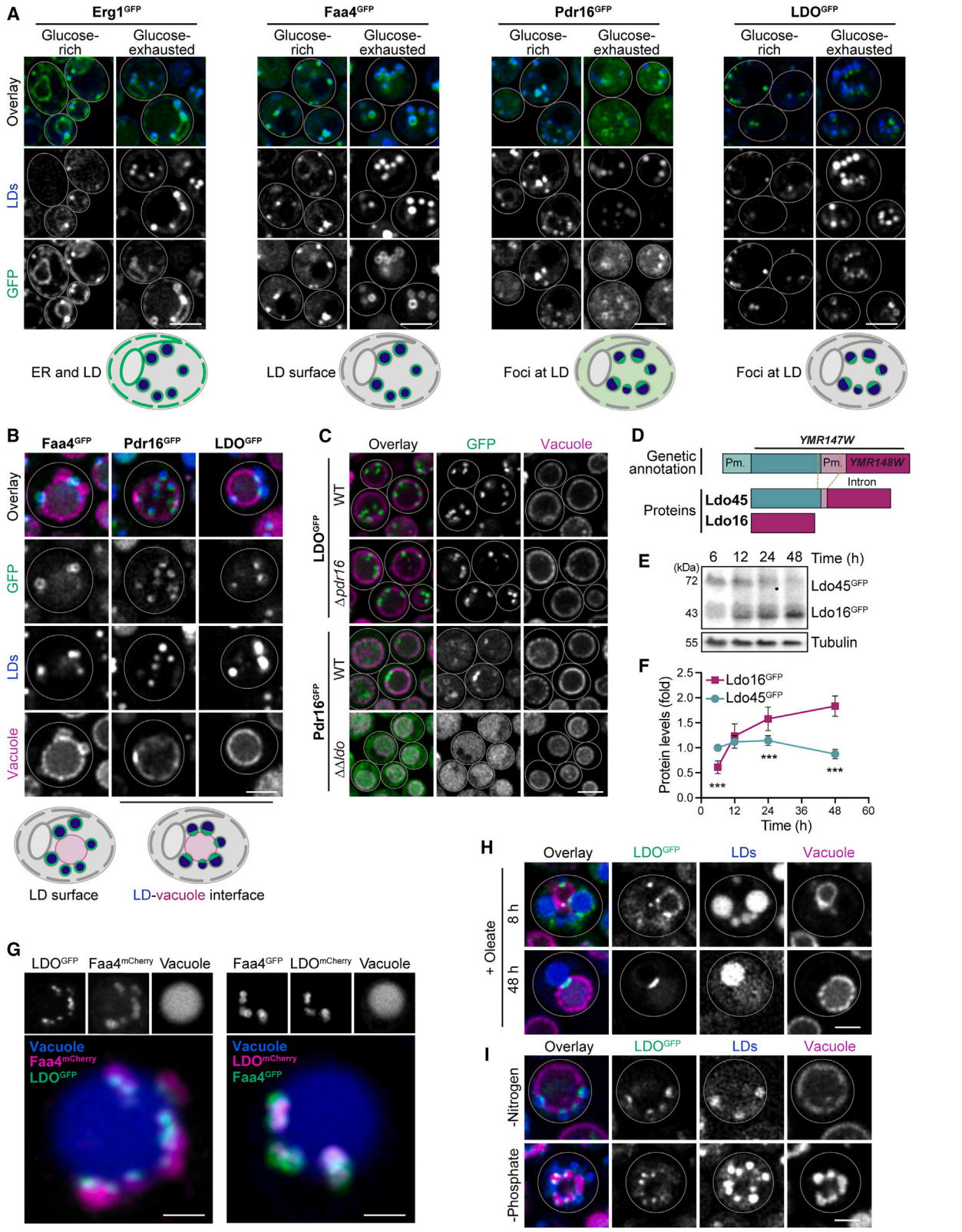

(legend on next page)

Please cite this article in press as: Álvarez-Guerra et al., LDO proteins and Vac8 form a vacuole-lipid droplet contact site to enable starvation-induced lipophagy in yeast, Developmental Cell (2024), https://doi.org/10.1016/j.devcel.2024.01.014

response to nutrient exhaustion (also see Diep et al.[35] submitted in parallel to this study). We demonstrate that the LD organization (LDO) proteins Ldo16 and Ldo45, encoded by overlapping genes and products of a splicing event,[36,37] attach LDs to the vacuolar membrane via Vac8, forming the vCLIP. Ldo16 was transcriptionally upregulated specifically upon nutrient depletion and anchored LDs to the vacuolar membrane via direct interaction of its C-terminal intrinsically disordered region with Vac8. Experimentally redirecting Vac8 to the nuclear membrane was sufficient to re-route LDs to juxtanuclear locations. In sum, we identify the molecular bridges that form vCLIP and show that this contact is critical for lipophagy and full lifespan extension via caloric restriction.

RESULTS

LDO proteins accumulate at the vacuole-LD interface upon nutrient exhaustion

The shift from rapid proliferation in nutrient-rich conditions to stationary phase upon nutrient exhaustion is associated with a metabolic switch that involves the transition from LD biogenesis to storage and gradual LD consumption. To assess how this transition affects LD-localized proteins, we followed the subcellular distribution of endogenous GFP fusions of the fatty acyl-coenzyme A (CoA) synthetase Faa4, the ergosterol biosynthesis enzyme Erg1, the phosphatidylinositol transfer protein Pdr16 and the LD organization proteins Ldo16/45.[36,37] We analyzed cells in glucose-rich conditions (8 h) and after prolonged incubation (48 h), resulting in gradual glucose exhaustion, a switch to respiratory metabolism and entry into stationary phase.[9] Under nutrient-rich conditions, all GFP fusions decorated the LDs, visualized using the neutral lipid stain monodansylpentane (MDH) (Figure 1A). As reported previously,[38] Erg1 also localized to the ER. In glucose-exhausted cells, Faa4 and Erg1 remained evenly distributed on the LD surface, while Pdr16 and in particular the LDO proteins formed distinct foci on LDs, mostly limited to one structure per LD. Simultaneous visualization of the vacuole using Vph1^{mCherry} revealed that these foci mark the vacuole-LD interface, suggesting that Pdr16 and the LDO proteins are redirected to contact sites between these organelles (Figure 1B). The targeting of the LDO proteins to the interface was not affected by genetic ablation of Pdr16 (Figure 1C). In contrast, the lack of both LDO proteins (ΔΔ*ldo*) prevented the accumulation of Pdr16 at these sites and resulted in its cytosolic distribution (Figure 1C), suggesting that the LDO proteins are required to recruit Pdr16 to these contacts. The LDO proteins are encoded by overlapping open reading frames (Figure 1D), and C-terminal tagging with GFP (referred to as LDO^{GFP}), thus allows the simultaneous visualization of both proteins (Figures 1A–1C). Imaging over time revealed that LDO^{GFP} rarely co-localized with the vacuole in exponentially growing cells but progressively formed foci at the vacuole after the diauxic shift (Figures S1A and S1B). Immunoblotting demonstrated that the expression of Ldo45 and Ldo16 was differentially affected by nutrient depletion (Figures 1E and 1F). Ldo16 protein levels progressively increased with time spent in stationary phase, while the levels of Ldo45 slightly decreased. Likewise, *LDO16* mRNA levels (but not *LDO45* levels) increased over time, indicating transcriptional upregulation of specifically Ldo16 (Figure S1C). Simultaneous visualization of Faa4^{mCherry} and LDO^{GFP} in glucose-exhausted cells demonstrated that the LDO proteins were targeted selectively to the vacuole-LD interface, while Faa4 remained evenly distributed at the LD surface, independent of which fluorescent tags were used (Figure 1G). Next, we ruled out that the starvation-induced targeting of LDO^{GFP} to the vacuole-LD interface was a simple consequence of increased LD size by expanding the LDs in exponentially growing cells on glucose-rich media using oleate supplementation.[39] Although oleate prominently enlarged the LDs, the LDO proteins remained distributed over the LD surface and only accumulated at the vacuole-LD interface in few, small foci when glucose was still available (Figure 1H). Again, also under oleate-supplemented conditions, entry into stationary phase redirected the LDO proteins to the expanded contact between the enlarged LDs and the vacuole. Furthermore, subjecting cells to phosphate restriction or acute nitrogen depletion resulted in the partitioning of the LDO proteins to the vacuole-LD interface (Figure 1I) and a specific increase of Ldo16 (Figures S1D–S1F). Collectively, this shows that limitation of the macronutrients glucose, nitrogen or phosphate induces Ldo16 expression and results in the specific targeting of the LDO proteins to the vacuole-LD interface, likely reflecting vCLIP that emerge in response to starvation.

LDO proteins target LDs to the vacuole to facilitate lipophagy

We directly tested whether LDO proteins are required for vCLIP formation. In wild-type (WT) cells, LDs were targeted to the vacuolar membrane (visualized via Vph1^{mCherry}) shortly after glucose exhaustion. Upon prolonged starvation, a large part of the LD population was engulfed into the vacuole via lipophagy

Figure 1. LDO proteins accumulate at the vacuole-LD interface upon nutrient exhaustion

(A) Micrographs of cells expressing Erg1^{GFP}, Faa4^{GFP}, Pdr16^{GFP}, or LDO^{GFP}, stained with MDH (LDs) at 8 h (glucose-rich) and 48 h (glucose-exhausted) of culturing in glucose media. Scale bars, 3 μm.

(B) Micrographs of cells expressing LDO^{GFP}, Pdr16^{GFP}, or Faa4^{GFP} and Vph1^{mCherry}, stained with MDH at 48 h. Scale bars, 3 μm.

(C) Micrographs of wild-type (WT), ΔΔ*ldo*, and Δ*pdr16* cells expressing Vph1^{mCherry} and either LDO^{GFP} or Pdr16^{GFP} at 48 h. Scale bars, 3 μm.

(D) Schematics of the genomic loci of *YMR147W*/*YMR148W* and promoters (Pm), encoding Ldo16 and Ldo45.

(E and F) Immunoblotting of protein extracts of cells expressing LDO^{GFP}. Representative blot (E) and corresponding quantifications, normalized to tubulin and depicted as fold of Ldo45^{GFP} at 6 h (F); mean ± SEM; n = 8.

(G) *Z* projection of glucose-exhausted cells (24 h) expressing LDO^{GFP} and Faa4^{mCherry} or LDO^{mCherry} and Faa4^{GFP}, stained with 7-amino-4-chloromethylcoumarin (CMAC; vacuole). Scale bars, 1 μm.

(H) Micrographs of cells expressing LDO^{GFP} and Vph1^{mCherry} grown in glucose media with 0.5% oleate, stained with MDH. Scale bars, 2 μm.

(I) Micrographs of cells expressing LDO^{GFP} and Vph1^{mCherry} upon nitrogen or phosphate depletion. Scale bars, 2 μm.

***$p < 0.001$.

See related Figure S1 and Table S6 for statistical analyses.

Please cite this article in press as: Álvarez-Guerra et al., LDO proteins and Vac8 form a vacuole-lipid droplet contact site to enable starvation-induced lipophagy in yeast, Developmental Cell (2024), https://doi.org/10.1016/j.devcel.2024.01.014

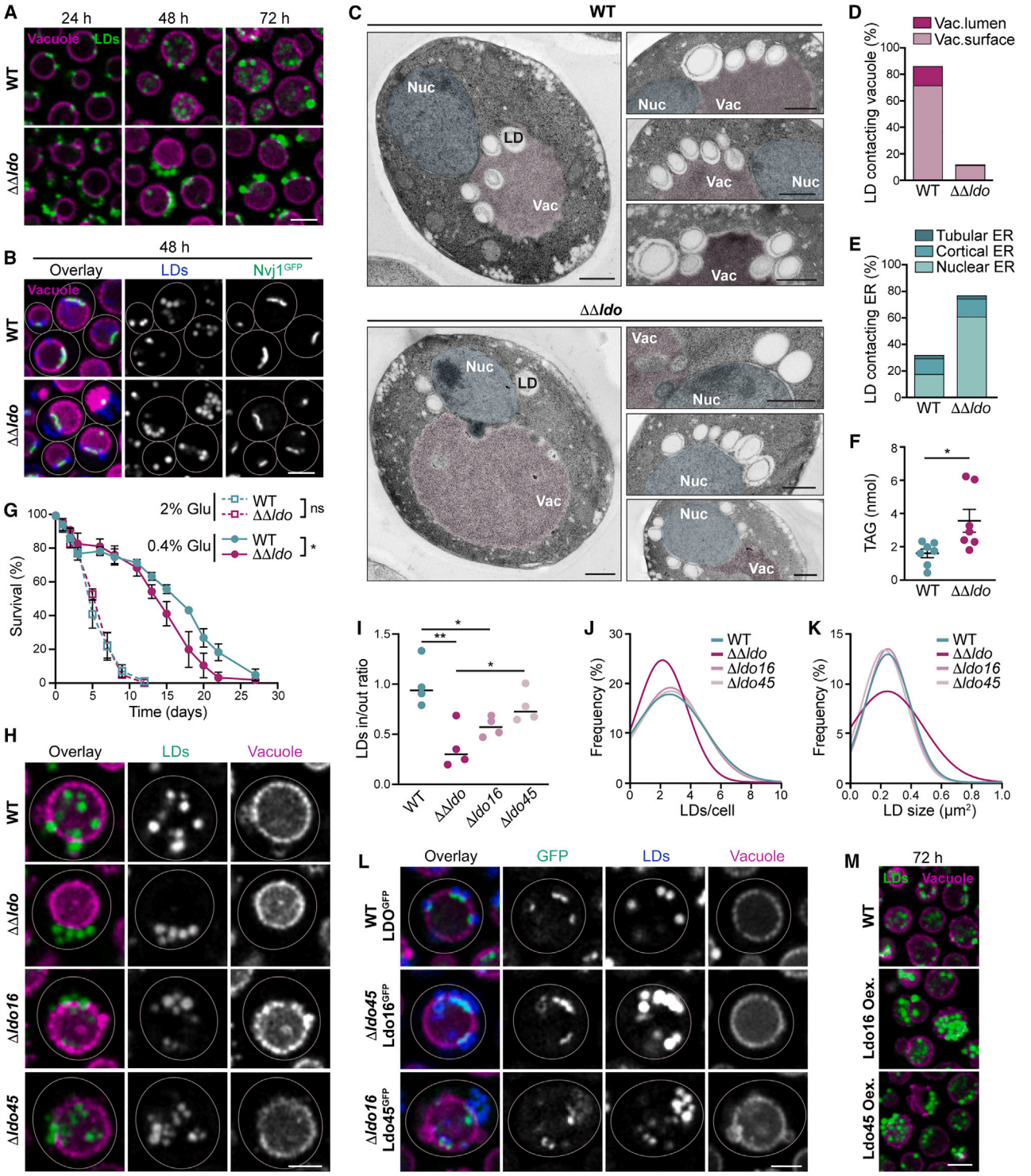

Figure 2. LDO proteins target LDs to the vacuole to facilitate lipophagy

(A) Micrographs of WT and ΔΔ*ldo* cells expressing Vph1^{mCherry}, stained with BODIPY493/503 (LDs). Scale bars, 3 μm.

(B) Micrographs of WT and ΔΔ*ldo* cells expressing Nvj1^{GFP} and Vph1^{mCherry}, stained with MDH. Scale bars, 3 μm.

(C) Electron micrographs of WT and ΔΔ*ldo* cells (32 h). Scale bars, 500 nm.

(D and E) Quantification of (C), depicting the number of LDs in contact with or inside the vacuole (D) and contacting the ER (E). Sections: n = 94 (WT), n = 127 (ΔΔ*ldo*).

(F) Triacylglycerol (TAG) levels in lysates from WT and ΔΔ*ldo* cells (48 h). Data points, mean (line), and SEM; n = 7.

(legend continued on next page)

Please cite this article in press as: Álvarez-Guerra et al., LDO proteins and Vac8 form a vacuole-lipid droplet contact site to enable starvation-induced lipophagy in yeast, Developmental Cell (2024), https://doi.org/10.1016/j.devcel.2024.01.014

(Figure 2A). In contrast, such starvation-induced lipophagy was absent in cells lacking both LDO proteins (ΔΔ*ldo*), which have already been proposed to contribute to lipophagy by yet unclear mechanisms.[37] In ΔΔ*ldo* cells, LDs remained clustered at one side of the vacuole, likely reflecting the nER and its contact to the vacuole at NVJs (Figure 2A). Indeed, visualization of the NVJs employing Nvj1^{GFP} demonstrated that in glucose-exhausted ΔΔ*ldo* cells, a few LDs remained associated with the NVJs, but most LDs clustered at the nER (Figures 2B and S2A). Transmission electron microscopy showed that in glucose-exhausted WT cells, more than 80% of LDs were closely attached to the vacuolar membrane at contact sites that reflect vCLIP, often already engulfed by the vacuole (Figures 2C and 2D). In contrast, in ΔΔ*ldo* cells, only 10% of the LDs contacted the vacuole, while 80% remained associated with the ER, mostly nER (Figures 2C–2E). This suggests a critical function of the LDO proteins in vCLIP formation and supports the notion that contact formation between LDs and the vacuole is a prerequisite for microlipophagy. Pdr16 as additional factor that is targeted to vCLIP was not required for lipophagy (Figure S2B). In line with a reduction of neutral lipid consumption via lipophagy, the lack of LDO proteins resulted in increased levels of TAGs in glucose-exhausted cells (Figure 2F). We reasoned that the impaired consumption of neutral lipids may reduce viability during caloric restriction, a regime known to induce longevity across species.[40] Similar to what was observed on standard media, the loss of vCLIP formation precluded lipophagy also when cells were grown into stationary phase on caloric restriction media containing 0.4% glucose (Figure S2C). Interestingly, inactivation of vCLIP compromised full lifespan extension induced by caloric restriction but did not affect cellular survival during chronological aging on control media with 2% glucose (Figure 2G).

To discriminate between Ldo16 and Ldo45 functions, we introduced selective deletion mutations to individually express either Ldo16 or Ldo45 from the chromosomal locus. Confocal microscopy and automated image quantification revealed that the individual loss of Ldo16 (but not of Ldo45) caused a slight reduction of vacuolar-LD engulfment upon glucose exhaustion, but not to the same extent as the simultaneous lack of both proteins (Figures 2H and 2I). Moreover, in ΔΔ*ldo* cells but not the single deletion mutants LDs displayed a different morphology, being fewer in number and prominently enlarged, suggesting that the presence of either LDO protein is sufficient to adjust the number and size of LDs to cellular needs (Figures 2J and 2K). In line with this, both Ldo16^{GFP} and Ldo45^{GFP} still efficiently accumulated at vCLIP to establish contact when expressed individually (Figure 2L). Furthermore, overexpression of either Ldo16 or Ldo45 triggered massive accumulation of LDs inside the vacuole, suggesting induction of lipophagy (Figures 2M and S2D). As the complete Ldo16 sequence is also present in Ldo45, we created a truncated Ldo45 variant that lacks the part shared with Ldo16. This Ldo45$^{\Delta C148}$ mutant still targeted the LDs but failed to attach LDs to the vacuole (Figures S2E and S2F). Taken together, both LDO proteins establish vCLIP by tethering the LDs to the vacuole via the shared Ldo16 domains, yet Ldo16 expression is selectively upregulated upon nutrient exhaustion.

The C-terminal disordered region of Ldo16 anchors LDs to the vacuole

Next, we generated a set of Ldo16 mutants to assign function to distinct protein regions. The N-terminus of Ldo16 likely corresponds to hydrophobic transmembrane α helixes (Figure 3A) and includes a proline-leucine-leucine-glycine (PLLG) motif as typical helix breaker. This might facilitate hairpin-like membrane insertion, characteristic for LD proteins that are targeted to LDs from the ER membrane.[41,42] In addition, Ldo16 is predicted to contain a cationic amphipathic helix (CAH; Figure 3B), again a common motif to target proteins to LDs.[43,44] The remainder of Ldo16 in its C-terminus is predicted to be an intrinsically disordered region, ending with a short α helix. We created a series of C- and N-terminally truncated Ldo16 variants as well as point mutants within the CAH, all ectopically expressed as GFP fusions in ΔΔ*ldo* cells (Figures 3C–3E). Immunoblotting confirmed the expression of all Ldo16 mutants, though modification of the predicted CAH impaired protein stability (Figure 3D). Assessing their subcellular localization demonstrated that the N-terminal hydrophobic region served as ER targeting signal, as its deletion prevented ER import (Ldo16$^{\Delta N49}$ and Ldo16$^{\Delta N72}$). Consistently, the Ldo16 variant containing only the N-terminal hydrophobic helixes (Ldo16$^{\Delta C98}$) was still imported into the ER. However, this mutant failed to associate with LDs, while a slightly longer variant that still contained the CAH (Ldo16$^{\Delta C54}$) was fully redirected to LDs (Figure 3C), demonstrating that the CAH is critical to target Ldo16 from the ER to LDs in the so-called ERTOLD pathway.[42] Exchanging 5 hydrophobic residues in the CAH with alanine did not prevent LD targeting, though accumulation of this Ldo16^{5xA} variant at the contact site was reduced (Figures 3C–3E). However, a stronger mutation of the CAH by inserting 2 glutamates resulted in severely compromised protein stability (Figure 3D) and ER retention (Figure 3C), supporting the notion that amphipathicity of the CAH contributes to Ldo16 targeting to LDs. Importantly, Ldo16$^{\Delta C54}$, which harbors a functional CAH but lacks the C-terminal disordered region, was efficiently redirected to LDs but decorated the complete LD surface

(G) Survival of WT and ΔΔ*ldo* cells during chronological aging, determined via flow cytometric quantification of propidium iodide staining. Cells were grown on standard (2% glucose) or caloric-restricted (0.4% glucose) media. Mean ± SEM; n = 4.
(H) Micrographs of WT, ΔΔ*ldo*, Δ*ldo16*, and Δ*ldo45* cells expressing Vph1^{mCherry}, stained with BODIPY493/503 at 48 h. Scale bars, 2 μm.
(I) Micrographs in (H) were used to quantify the ratio of BODIPY intensity inside/outside the vacuole. Line (mean); n = 4, 200–500 cells per n.
(J and K) Micrographs in (H) were used to quantify LD number per cell frequencies (J) and LD size frequencies (K) fitted to a gaussian distribution. 200-500 cells (J) and 800–1,500 LDs (K) per genotype.
(L) Micrographs of WT cells expressing LDO^{GFP} and Δ*ldo45* and Δ*ldo16* cells expressing Ldo16^{GFP} or Ldo45^{GFP}. Cells expressed Vph1^{mCherry}, were stained with MDH, and analyzed at 48 h. Scale bars, 2 μm.
(M) Micrographs of WT and ΔΔ*ldo* cells ectopically overexpressing Ldo45 or Ldo16, expressing Vph1^{mCherry}, stained with BODIPY493/503 and analyzed at 72 h. Scale bars, 3 μm.
*p < 0.05, **p < 0.01.
See related Figure S2 and Table S6 for statistical analyses.

Please cite this article in press as: Álvarez-Guerra et al., LDO proteins and Vac8 form a vacuole-lipid droplet contact site to enable starvation-induced lipophagy in yeast, Developmental Cell (2024), https://doi.org/10.1016/j.devcel.2024.01.014

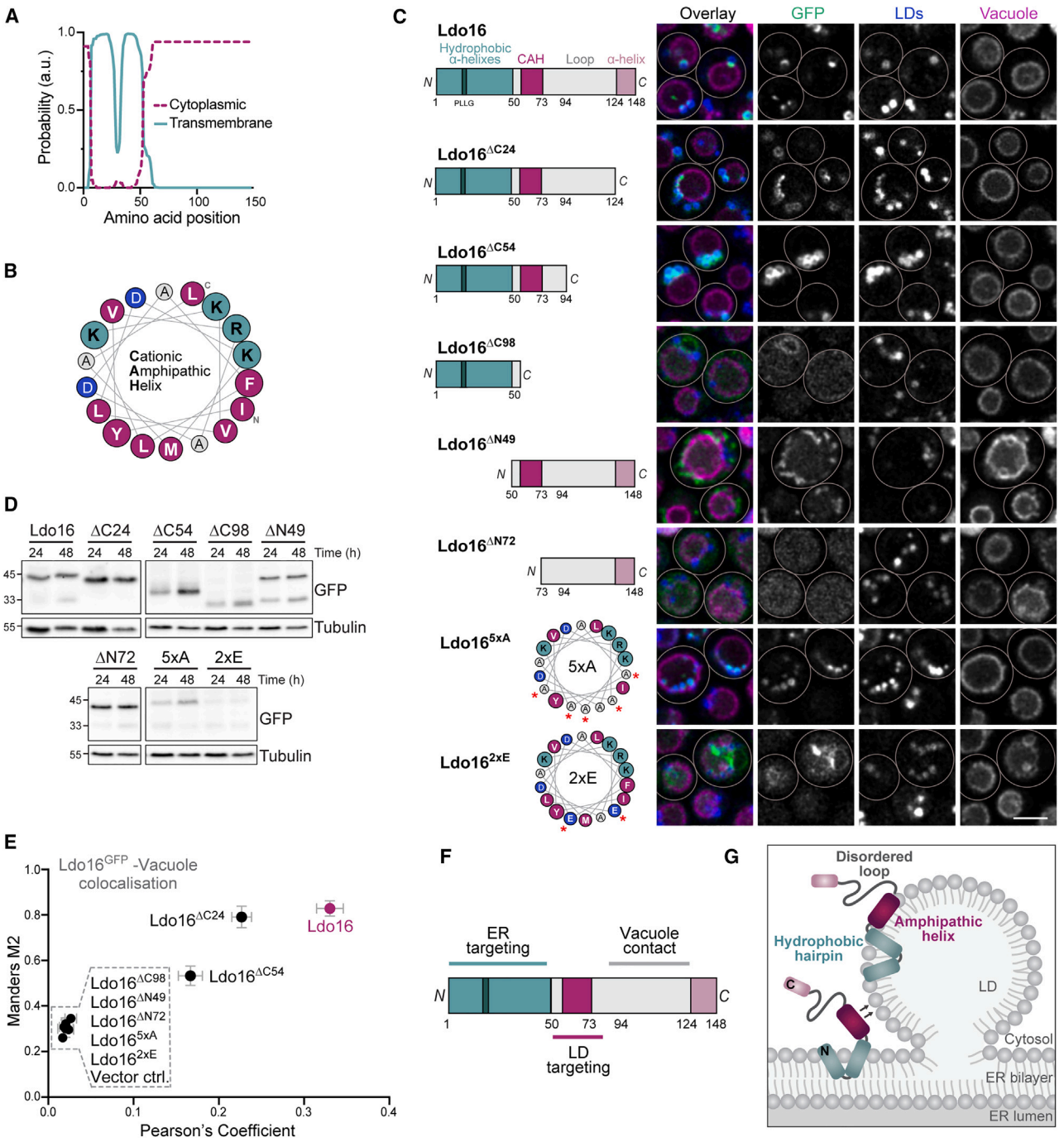

Figure 3. The C-terminal disordered region of Ldo16 anchors LDs to the vacuole

(A) Hydrophobicity plot of Ldo16 protein sequence using Phobius.

(B) α helix prediction by HeliQuest of putative Ldo16 cationic amphipathic helix (CAH). Hydrophobic residues (magenta), positively charged residues (turquoise).

(C) Schematics of generated Ldo16 mutants and micrographs upon ectopic expression of Ldo16^{GFP} mutants in ΔΔ*ldo* cells expressing Vph1^{mCherry}, stained with MDH (48 h). Scale bars, 3 μm.

(D) Immunoblotting of protein extracts from ΔΔ*ldo* cells expressing Ldo16^{GFP} variants.

(E) Co-localization analysis of Ldo16^{GFP} variants with the vacuole (Vph1^{mCherry}) from micrographs in (C). Mean ± SEM; n = 6–10, at least 30 cells per n.

(F and G) Schematics of Ldo16 domains (F) and Ldo16 integration into the LD monolayer (G).

Please cite this article in press as: Álvarez-Guerra et al., LDO proteins and Vac8 form a vacuole-lipid droplet contact site to enable starvation-induced lipophagy in yeast, Developmental Cell (2024), https://doi.org/10.1016/j.devcel.2024.01.014

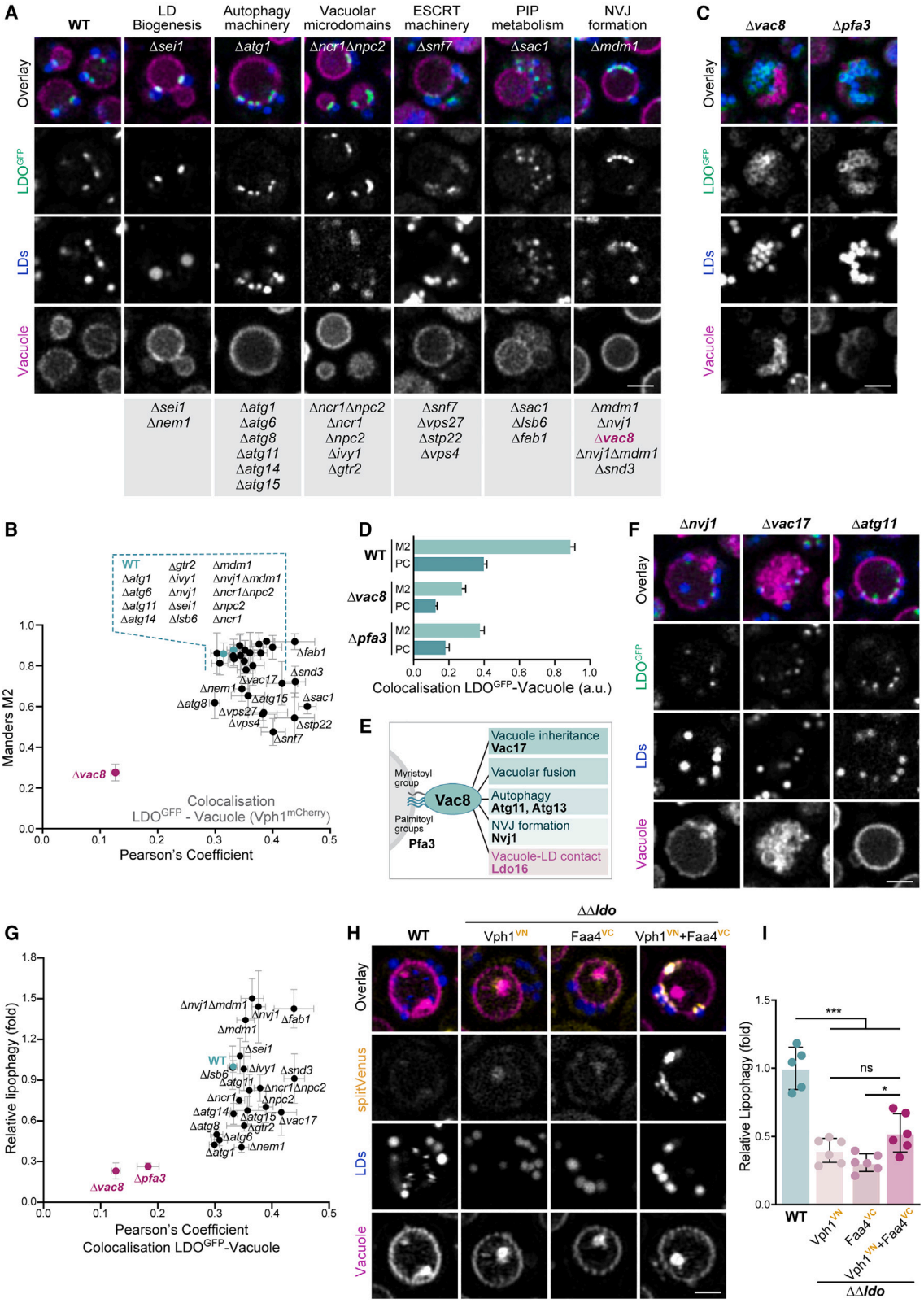

(legend on next page)

Please cite this article in press as: Álvarez-Guerra et al., LDO proteins and Vac8 form a vacuole-lipid droplet contact site to enable starvation-induced lipophagy in yeast, Developmental Cell (2024), https://doi.org/10.1016/j.devcel.2024.01.014

instead of accumulating at vCLIP. In addition, the complete LD population remained attached to one side of the vacuole, likely reflecting the nER (Figure 3C), demonstrating that the C-terminus of Ldo16 is critical for contact formation. Removing only the short α helix (24 C-terminal residues) did not prevent accumulation at vCLIP, indicating that it is the intrinsically disordered region that is essential for Ldo16 function in contact formation. Collectively, this suggests that Ldo16 is targeted to the ER via its N-terminal hydrophobic region, is redirected from the ER membrane to the LD surface via its CAH and attaches to the vacuolar membrane via the intrinsically disordered region in its C terminus to establish vCLIP (Figures 3F and 3G).

Vac8 is required for vCLIP formation

To identify cellular processes and molecular determinants involved in Ldo16-mediated LD-vacuole tethering, we examined LDO^{GFP} localization in a set of mutants with established functions in LD biosynthesis, autophagy, the endosomal sorting complex required for transport (ESCRT), NVJ formation and vacuolar membrane lipid composition. All mutants, expressing Vph1^{mCherry} to visualize the vacuole and stained with MDH, were grown to glucose exhaustion and assessed microscopically for contact formation (Figures 4A and S3A), scored as co-localization between LDO^{GFP} and Vph1^{mCherry} (Figure 4B). The LDO proteins have previously been shown to interact with seipin (Sei1) at the ER membrane to support LD biogenesis in growing cells.[36,37] However, the lack of seipin did not compromise LDO^{GFP} targeting to the contact sites. Likewise, neither genetic inactivation of autophagy nor impairment of endosomal protein sorting via deletion of genes coding for ESCRT components, which have been suggested to contribute to lipophagy,[30,31,33,45] altered LDO-mediated tethering of LDs to the vacuole. The formation of L_o microdomains on the vacuolar membrane has also been associated with stationary phase lipophagy,[33,34,46] but defective L_o domain formation did not prevent vCLIP formation. Similarly, changes in phosphatidylinositol metabolism had no effect on contact formation despite altered vacuolar morphology (Figures 4A, 4B, and S3A). Finally, we tested whether NVJs are required for LD tethering to the vacuole, as the LDO proteins have been shown to decorate a LD subpopulation associated with the NVJs.[36,37] LDO-mediated tethering was unaffected in cells lacking either Nvj1 or Mdm1, bridging proteins required for NVJ formation,[10,47] or lacking the NVJ regulator Snd3.[9] Importantly, one strain showed severely impaired vCLIP formation: the loss of the vacuolar protein Vac8 prevented LDO^{GFP} targeting to the vacuolar-LD interface, resulting instead in its spreading over the complete LD surface (Figure 4C). Quantification of LDO^{GFP}-Vph1^{mCherry} co-localization supported the absence of vCLIP in Δ*vac8* cells (Figures 4B and 4D). In line with a critical function of Vac8 in recruiting LDs to the vacuole, cells lacking the palmitoyltransferase Pfa3, which lipidates Vac8 to attach it to the vacuolar membrane,[48] resembled Δ*vac8* cells (Figures 4C and 4D). The armadillo (ARM) repeat protein Vac8 has previously been linked to lipophagy[31] and contributes to multiple cellular processes via direct interaction with distinct proteins, including Nvj1 to tether the vacuole to the nER at NVJ,[10] Vac17 to facilitate vacuole inheritance,[49] as well as Atg11 and Atg13 to support phagophore assembly during selective and bulk macroautophagy, respectively.[50,51] The lack of any of these Vac8 interactors did not preclude vCLIP formation (Figure 4F), suggesting that it is the absence of Vac8 per se rather than the impairment of associated processes that prevents vCLIP formation. Overall, these data demonstrate that Vac8 is required to recruit LDs to the vacuole.

vCLIP formation is critical but not sufficient for lipophagy

To assess whether the formation of vCLIP is sufficient to trigger vacuolar uptake of LDs, we quantified lipophagy in the deletion mutants analyzed for changes in vCLIP formation. Cells lacking ESCRT components were omitted, as a clear discrimination between LDs inside or outside the highly fragmented vacuole was not possible. Plotting lipophagy as a function of LDO^{GFP} co-localization with the vacuolar membrane revealed that uniquely the lack of Vac8 and its palmitoyltransferase Pfa3 precluded vCLIP formation as well as lipophagy (Figure 4G). Despite efficient vCLIP formation, cells lacking regulators of macroautophagy such as Atg1, Atg6, and Atg8, all previously linked to lipophagy,[30] displayed reduced vacuolar LD uptake (Figure 4G). Similarly, the loss of Atg14, which has been suggested to mediate lipophagy through re-distribution to the vacuolar surface,[30] reduced LD uptake to some extent without affecting vCLIP formation (Figure 4G). Microscopic analysis demonstrated that Atg14^{GFP} targeted the rim of some, but not all, vCLIP established by the LDO proteins when cells were grown into glucose exhaustion (Figure S3B). Collectively, this indicates that key regulators of autophagy are not required for vCLIP formation but contribute to vacuolar LD uptake.

Interestingly, we observed that NVJ inactivation impacted on lipophagy but not vCLIP formation. Compromising NVJ formation by genetic ablation of Nvj1 or Mdm1 increased the vacuolar uptake of LDs (Figure 4G). Mdm1 has been suggested to mediate a three-way connection between ER, vacuole and LDs to support localized LD biogenesis at NVJ in proximity to the vacuole.[12,47,52] Thus, we tested for co-localization of Mdm1 and the

Figure 4. Vac8 is required for vCLIP formation

(A–D) Micrographs of WT and indicated mutants expressing LDO^{GFP} and Vph1^{mCherry}, stained with MDH and analyzed at 48 h (A and C) and corresponding co-localization analysis of Vph1^{mCherry} with LDO^{GFP} (B and D). Mean ± SEM; n = 4–10, at least 30 cells per n. Scale bars, 2 μm.

(E) Schematics of Vac8 functions and interactors.

(F) Micrographs of cells lacking Vac8 interactors and expressing LDO^{GFP} and Vph1^{mCherry}, stained with MDH at 48 h. Scale bars, 2 μm.

(G) Relative lipophagy, determined by quantifying the ratio of MDH intensity inside/outside the vacuole, plotted against the Pearson's coefficient for Vph1^{mCherry} and LDO^{GFP} co-localization as in (B). Mean ± SEM; n = 4–10, at least 30 cells per n.

(H) Micrographs of WT and Δ*Δldo* cells expressing one or both splitVenus fragments fused to Vph1 (Vph1^{VN}) or Faa4 (Faa4^{VC}), stained with FM4-64 and MDH at 48 h. Scale bars, 2 μm.

(I) Micrographs in (H) were used to quantify the ratio of MDH intensity inside/outside the vacuole. Mean ± SEM; n = 5–6, with 40–50 cells per n.

*$p < 0.05$, ***$p < 0.001$, ns, not significant.

See related Figure S3 and Table S6 for statistical analyses.

Please cite this article in press as: Álvarez-Guerra et al., LDO proteins and Vac8 form a vacuole-lipid droplet contact site to enable starvation-induced lipophagy in yeast, Developmental Cell (2024), https://doi.org/10.1016/j.devcel.2024.01.014

CellPress
OPEN ACCESS

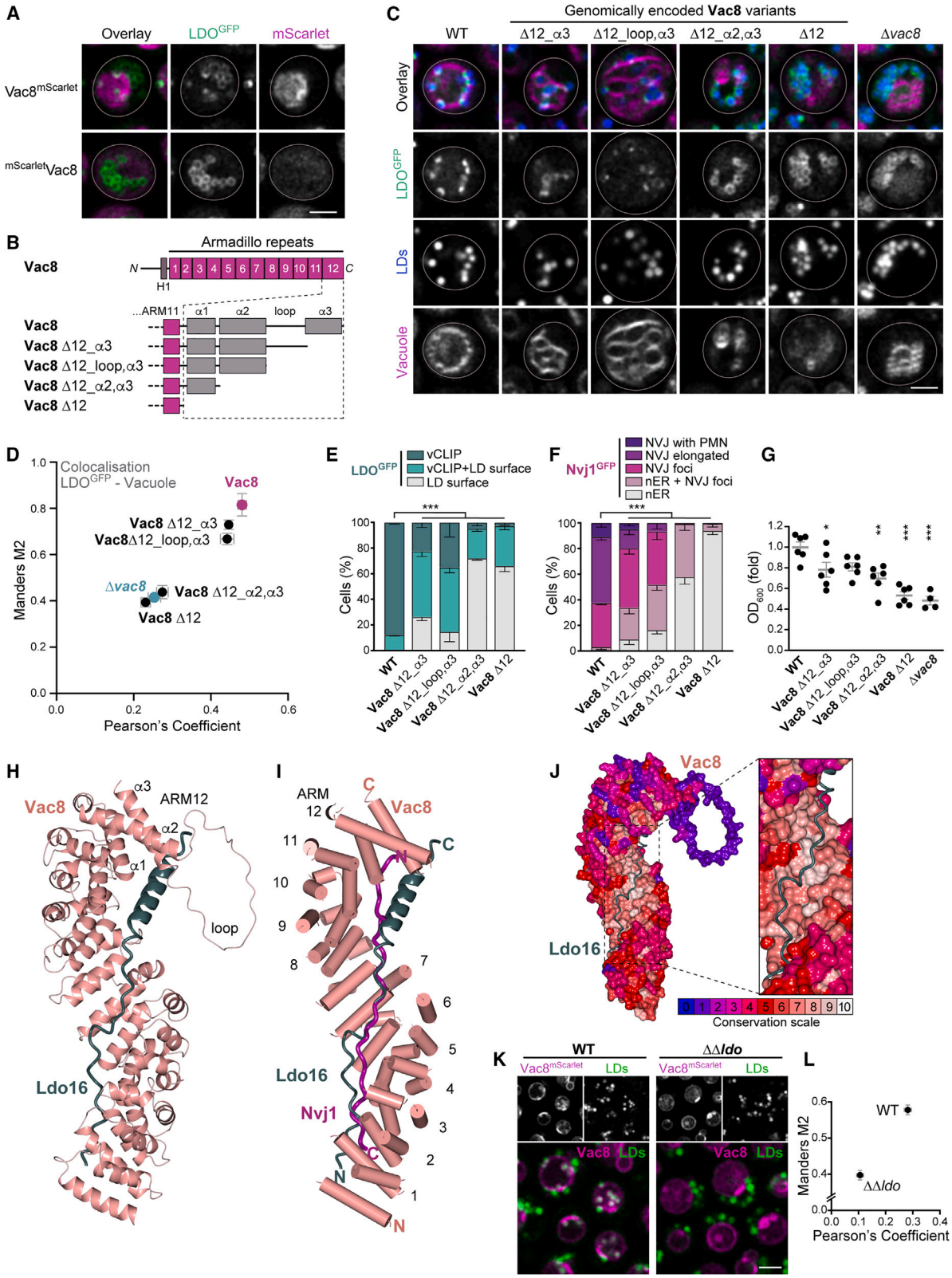

(legend on next page)

Please cite this article in press as: Álvarez-Guerra et al., LDO proteins and Vac8 form a vacuole-lipid droplet contact site to enable starvation-induced lipophagy in yeast, Developmental Cell (2024), https://doi.org/10.1016/j.devcel.2024.01.014

LDO proteins and indeed detected Mdm1^{GFP} in close proximity to a subpopulation of vCLIP (Figure S3B). Still, Mdm1 was dispensable for vCLIP formation (Figures 4A and 4B), suggesting a potential regulatory function at the ER-vacuole-LD interface.

Finally, we assessed whether bringing the LDs to the surface of the vacuole was sufficient to induce lipophagy even in absence of the LDO proteins. To this end, we fused Faa4 and Vph1 to splitVenus fragments and established the reconstitution of splitVenus via bimolecular fluorescence complementation (Figure 4H). The enforced tethering of LDs to the vacuolar surface did not restore the lipophagy defect of ΔΔ*ldo* cells, suggesting that the LDO proteins provide lipophagic function beyond mere tethering (Figure 4I).

Modification of the C terminus of Vac8 disrupts vCLIP formation

Next, we tested for co-localization of endogenously expressed LDO^{GFP} and Vac8^{mScarlet} (Figure 5A). C-terminal tagging of Vac8 has extensively been used in the field, mostly without impairing Vac8 functions,[53] and we confirmed that mScarlet-tagging resulted in a functional protein based on growth (Figures S4A and S4B). Interestingly, the C-terminal tagging of Vac8 triggered the re-distribution of LDO^{GFP} to cover the complete LD surface and precluded vCLIP formation, a phenotype reminiscent of its distribution in Δ*vac8* cells (Figures 4C and 5A). A similar disruption of contact formation was observed when using HA as alternative epitope (Figure S4C), while N-terminal tagging caused the loss of Vac8, most likely due to interference with its palmitoylation and thus defective membrane anchoring (Figure 5A). The interactions of Vac8 with Nvj1 and Atg13 have previously been studied at the structural level, showing that the last ARM repeat at its C terminus (ARM12) is not involved in the interaction.[54,55] As C-terminal tagging selectively disrupted vCLIP formation while not affecting other Vac8 functions, we created a series of genomically encoded C-terminal truncations of Vac8, successively deleting the α helixes of ARM12 (Figure 5B). We monitored LDO^{GFP} localization in combination with the vacuole (using FM4-64) and LDs (using MDH) (Figure 5C) and scored for LDO^{GFP}—vacuole co-localization (Figure 5D) as well as for accumulation of LDO^{GFP} at vCLIP versus the entire LD surface (Figure 5E). The truncation of the last α helix (α3) only slightly compromised contact formation (Figures 5D and 5E), although vacuolar morphology was already affected (Figure 5C). Further truncation of ARM12 disrupted contact formation, resulting in the spreading of LDO^{GFP} across the complete LD surface, reminiscent of Δ*vac8* cells, and prominent vacuolar fragmentation (Figures 5C–5E). To assess whether these C-terminal truncations of Vac8 would also interfere with well-established interactions, we used Nvj1^{GFP} to monitor NVJ formation in cells harboring the Vac8 variants at the endogenous locus. This revealed a similar pattern of disruption of Vac8 binding to its partner, here Nvj1 (Figures 5F and S4D). The progressive loss of Vac8 interactions upon truncation of the α helixes of ARM12 correlated well with the extent of growth arrest (Figures 5G and S4E). As ARM12 does not directly contribute to the interaction interface of the Vac8-Nvj1 complex, determined by crystallography,[54,55] it is likely that these C-terminal truncations impair a general aspect of protein structure. The regions of both Nvj1 and Atg13 that interact with Vac8 are disordered loops near their C-termini.[54,55] Despite these sharing little sequence homology, both loops run as extended peptides along the minor groove of the ARM repeat superhelix. We used ColabFold[56] to examine if an interaction surface in Vac8 could be predicted for Ldo16. Of the five best models obtained from full-length sequences of both proteins, all showed a portion of the disordered C terminus of Ldo16 in contact with the minor groove of the Vac8 superhelix (Figure 5H), with the top ranked model having the majority of the C terminus of Ldo16 making multiple contacts with Vac8 (22 of 34 residues between 104 and 137 had $\geq$8 contacts defined as atom centers $\leq$4 Å apart). Notably, the predicted position of Ldo16 is the same as that previously found for Nvj1 (Figure 5I). Thus, Ldo16 and Nvj1 might bind to the same Vac8 groove, potentially competing for Vac8 interaction when Ldo16-decorated LDs enrich at the NVJs shortly after glucose exhaustion. The elongated interaction surface along the minor groove of Vac8 is well conserved despite being spread across multiple ARM repeats (Figure 5J). The five ColabFold models aligned Ldo16 in the same direction, which was parallel to Vac8 (i.e., opposite to the direction of Nvj1 and Atg13). According to this prediction, the C-termini of Vac8 and Ldo16 would be in close proximity, and insertion of C-terminal tags simultaneously on both proteins might interfere with their interaction. To test this, we monitored LD localization in a strain equipped with Vac8^{mScarlet} and untagged LDO proteins. Indeed, Vac8^{mScarlet} accumulated at sites where LDs made contact with the vacuole when the LDO proteins were untagged (Figures 5K

Figure 5. Modification of the C terminus of Vac8 disrupts vCLIP formation

(A) Micrographs of cells expressing LDO^{GFP} and Vac8, C- or N-terminally fused to mScarlet, after 48 h. Scale bars, 2 μm.

(B) Schematics of the armadillo (ARM) repeat protein Vac8, highlighting ARM12 and generated Vac8 mutants.

(C) Micrographs of WT, Δ*vac8* and cells endogenously expressing truncated Vac8 variants shown in (B) and LDO^{GFP}, stained with MDH and FM4-64 at 48 h. Scale bars, 2 μm.

(D) Co-localization analysis of FM4-64 (vacuole) with LDO^{GFP} in cells from (C). Mean ± SEM; n = 5–9, at least 30 cells per n.

(E) Quantification of cells in (C) according to LDO^{GFP} distribution. At least 230 cells per genotype.

(F) Quantification of cells expressing Vac8 mutants according to Nvj1^{GFP} distribution from micrographs in Figure S4D. At least 90 cells per genotype.

(G) Optical density of WT, Δ*vac8* and cells expressing Vac8 mutants after 10 h. Mean ± SEM; n = 6.

(H) Predicted interaction model (ColabFold) of Vac8 and Ldo16.

(I) Predicted position of Ldo16 compared with the position established for Nvj1.

(J) Structural model of Vac8 in conservation scale with predicted interaction surface of Ldo16.

(K and L) Micrographs of WT and ΔΔ*ldo* cells expressing Vac8^{mScarlet}, stained with BODIPY493/503 at 48 h (K), and corresponding co-localization (L). Scale bars, 2 μm. Mean ± SEM; n = 10–11, at least 25 cells per n.

*p < 0.05, **p < 0.01, ***p < 0.001.

See related Figure S4 and Table S6 for statistical analyses.

Please cite this article in press as: Álvarez-Guerra et al., LDO proteins and Vac8 form a vacuole-lipid droplet contact site to enable starvation-induced lipophagy in yeast, Developmental Cell (2024), https://doi.org/10.1016/j.devcel.2024.01.014

and 5L). Overall, these results suggest that (1) Vac8 is recruited to vCLIP and (2) C-terminal tagging of both proteins at the same time interferes with vCLIP formation. Clustering of Vac8 at LDs was absent in ΔΔ*ldo* cells, while clear Vac8 patches at NVJs were visible (Figure 5K), demonstrating that the LDO proteins are critical for Vac8 recruitment to vCLIP.

Vac8 interacts with Ldo16 and recruits LDs to cellular membranes

We used electron microscopy and immunogold labeling to test for a specific targeting of native Vac8 to vCLIP in glucose-exhausted WT cells. As expected, we detected Vac8 at the entire vacuolar membrane, with an enrichment at the NVJs (Figures 6A and 6B). Of note, Vac8 in addition clustered at vacuolar membrane regions that made contact with LDs and that often were in the process of engulfing LDs, suggesting that Vac8 indeed accumulates at vCLIP. Next, we probed for a direct interaction between Vac8 and Ldo16. We co-expressed glutathione-S-transferase-tagged Vac8 (GST-Vac8) with the soluble form of Ldo16 ($Ldo16^{\Delta N49}$ lacking the hydrophobic membrane domain; Figure 3C), fused to the solubility tag Sumo, in *E. coli*. GST pull-down experiments revealed a direct interaction between Vac8 and Ldo16, with approximately 40% of the total expressed Ldo16 protein co-purifying with GST-Vac8 (Figures 6C and 6D). Thus, the C-terminal part of Ldo16 is sufficient to form a complex with Vac8.

To test whether Vac8 serves as a tether protein that recruits LDs to cellular membranes, we reconstituted this process at the nER, employing a previously established tethering system.[50] Fusion of the N-terminal half of Nvj1 to Vac8ΔN, a variant that lacks the domains necessary to attach it to the vacuolar membrane, drives the attachment of Vac8ΔN to the nuclear envelope.[50] Importantly, ectopic expression of this nER-attached Vac8 in Δ*vac8* cells recruited LDs to the nER (Figure 6E). The LDO proteins and Vac8 accumulated at concave nER patches in which attached LDs were buried, suggesting that Vac8 is the single necessary and sufficient component of the vacuolar membrane that recruits LDs (Figures 6E and 6F). Notably, targeting LDs to the nER resulted in a strong deformation of the nER at sites enriched in LDO and Vac8, raising the possibility that the interactions of these proteins at the interface between LDs and cellular membranes support membrane bending to push LDs inward. As a positive control to validate chimera functionality, Vac8ΔN was fused to Vph1 to retain it at the vacuolar membrane, which predicably resulted in co-localization of LDO^{GFP} and Vac8 at the vacuole and LD attachment. Collectively, these data suggest that Vac8 interacts with LDO proteins to establish vCLIP and is sufficient to recruit LDs to an organelle, thus fulfilling the formal criteria of a membrane contact site tether.[1]

Proteolysis associated with lipophagy depends on vCLIP

We quantitatively assessed the impact of defective vCLIP formation on lipophagic activity associated with proteolytic breakdown of cargo. To this end, GFP liberation from $Faa4^{GFP}$ by vacuolar proteases was followed by immunoblotting. $Faa4^{GFP}$ levels progressively decreased with time spent in glucose exhaustion, which was accompanied by the simultaneous increase of free GFP (Figures 7A–7C). Microscopic analysis confirmed vacuolar uptake and breakdown of $Faa4^{GFP}$-decorated LDs (Figure S5A). Genetic ablation of the LDO proteins reduced the level of free GFP but not $Faa4^{GFP}$, suggesting a drop in lipophagic activity (Figures 7A–7D). Notably, no GFP liberation was detectable in cells devoid of Vac8 (Figure 7D). Consistently, Δ*vac8* cells did not sequester LDs into the vacuole and displayed an increase in LD size comparable to ΔΔ*ldo* cells (Figures 7E–7G). While loss of Vac8 completely blocked lipophagy, ΔΔ*ldo* cells still maintained residual lipophagic activity. Here, some LDs were still engulfed into the vacuole in particular upon prolonged glucose exhaustion (72 h) (Figure 7F), and lipophagy-associated proteolytic GFP liberation from $Faa4^{GFP}$ was reduced but not completely blocked (Figures 7A–7D). This suggests that LDO-independent mechanisms for lipophagy exist that still require Vac8.

Disruption of vCLIP induces NVJ expansion and PMN

Vac8 is a key resident of both NVJs and vCLIP, raising the possibility of cross-talk via this shared and perhaps limiting component. Indeed, inhibition of NVJ formation by removing Nvj1 or both Nvj1 and Mdm1 resulted in increased uptake of LDs into the vacuole (Figures 4G, 7E, and 7F). Additional loss of the LDO proteins blocked this uptake. Vice versa, the inactivation of vCLIP in ΔΔ*ldo* cells affected NVJ size and shape, resulting in expanded NVJs that frequently appeared fragmented due to ongoing piecemeal microautophagy of the nucleus (PMN) (Figures 7H and 7I). This special form of microautophagy occurs only at the NVJs and is characterized by vacuolar membrane invagination that leads to the pinching-off of vesicles carrying portions of nuclear cargo for subsequent vacuolar degradation.[57] Electron microscopy demonstrated a 3-fold increase of sections with PMN vesicles upon inactivation of vCLIP, and often multiple PMN vesicles formed simultaneously along the expanded NVJs (Figures 7J and 7K). Confocal microscopy using $Nvj1^{GFP}$ confirmed a prominent increase of PMN in ΔΔ*ldo* cells (Figures 7L and 7M). Likewise, immunoblotting demonstrated increased vacuolar GFP liberation from $Nvj1^{GFP}$ in these cells, suggesting increased cargo turnover via PMN upon vCLIP inactivation (Figures S5B–S5D). Conceptually, the mutually negative regulation of NVJs and vCLIP is likely caused by a tug-of-war for limiting Vac8 but may also involve compensatory cellular responses to maintain needed lipid flux to the vacuole. These results point to a functional link between the NVJ and the vCLIP, both of which are established by Vac8 at the vacuolar membrane and metabolically regulated.

DISCUSSION

The mobilization of fat stored in LDs plays a central role in both physiological lipid metabolism and human pathology.[16,58,59] Lipophagy, one of two routes for LD consumption, enables eukaryotic cells to use lipids as an energy source under nutrient deprivation. This route requires docking of LDs to the lysosome/vacuole before uptake by so far unknown means. Here, we have identified the molecular machinery that tethers LDs to the vacuole to enable LD consumption via lipophagy in yeast. The LD-localized LDO proteins attach to the vacuolar ARM repeat protein Vac8 to form vCLIP, the vacuole-LD contact site. We demonstrate that vCLIP emerges specifically upon nutrient

Please cite this article in press as: Álvarez-Guerra et al., LDO proteins and Vac8 form a vacuole-lipid droplet contact site to enable starvation-induced lipophagy in yeast, Developmental Cell (2024), https://doi.org/10.1016/j.devcel.2024.01.014

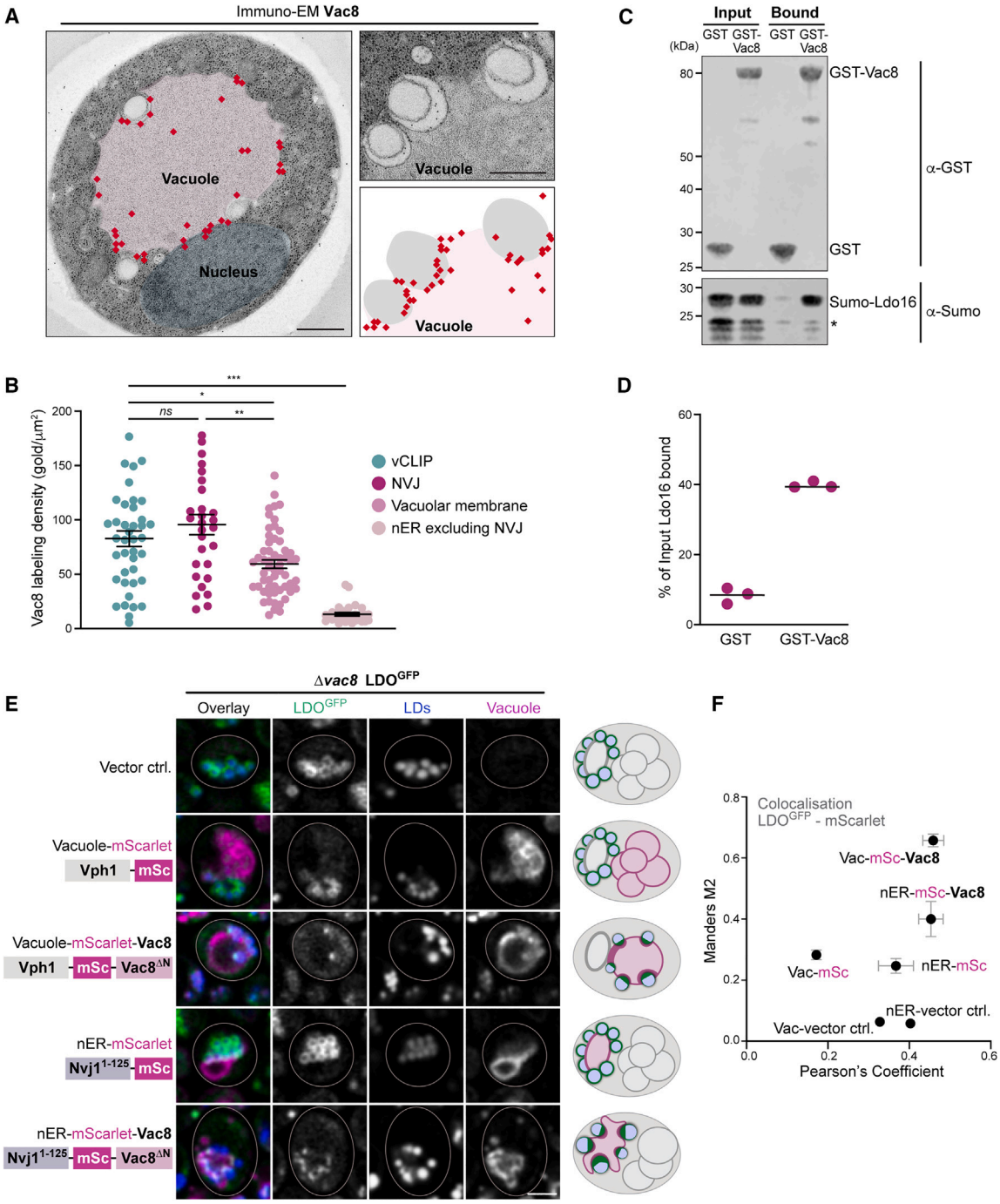

Figure 6. Vac8 interacts with Ldo16 and recruits LDs to cellular membranes

(A) Electron micrographs of immunogold labeling of WT cells (32 h) using a Vac8 antibody, with gold particles (red) and labeling density model. Scale bars, 500 nm.

(B) Quantification of Vac8 labeling density from (A) at indicated vacuolar membrane regions. Data points, mean (line) and SEM; n = 57 sections.

(C and D) Immunoblot of glutathione-S-transferase (GST) pull-down (bound) from total protein extracts (input) from *E. coli* co-expressing the soluble form of Ldo16 ($Ldo16^{\Delta N49}$) fused to Sumo and GST or GST-Vac8. Representative blots (C) and corresponding quantification (D). Data points with mean (line); n = 3. *indicates Ldo16 degradation.

(E) Micrographs of Δ*vac8* cells expressing LDO^{GFP} and ectopically expressing indicated constructs. Schematics depict distribution of Vac8 and LDO. Scale bars, 2 μm.

(F) Co-localization analysis of LDO^{GFP} with mScarlet from micrographs in (E). Mean ± SEM; n = 6, at least 30 cells per n.

*p < 0.05, **p < 0.01, ***p < 0.001.

See Table S6 for statistical analyses.

Please cite this article in press as: Álvarez-Guerra et al., LDO proteins and Vac8 form a vacuole-lipid droplet contact site to enable starvation-induced lipophagy in yeast, Developmental Cell (2024), https://doi.org/10.1016/j.devcel.2024.01.014

CellPress
OPEN ACCESS

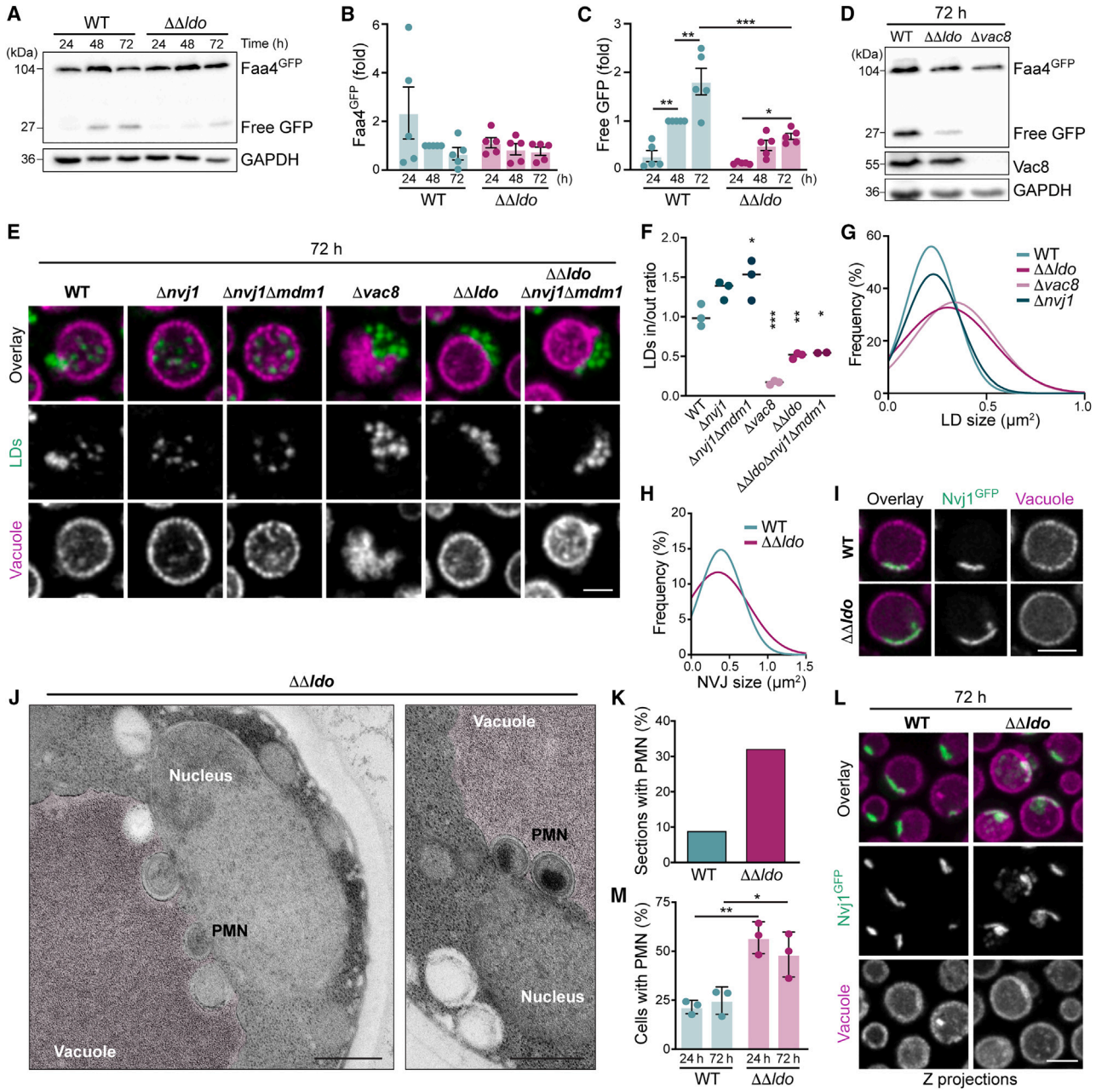

Figure 7. Disruption of vCLIP induces NVJ expansion and piecemeal microautophagy of the nucleus

(A–C) Immunoblotting of protein extracts from WT and ΔΔ*ldo* cells expressing Faa4^{GFP}. Representative immunoblots (A) and corresponding quantification of full-length Faa4^{GFP} (B) and free GFP liberated from Faa4^{GFP} (C), normalized to GAPDH. Mean ± SEM; n = 6.

(D) Immunoblot of protein extracts from WT, ΔΔ*ldo*, and Δ*vac8* cells expressing Faa4^{GFP}.

(E) Micrographs of WT and indicated mutants expressing Vph1^{mCherry}, stained with BODIPY493/503 at 72 h. Scale bars, 2 μm.

(F) Quantification of the ratio of BODIPY intensity inside/outside the vacuole from micrographs in (E). Line (mean); n = 3, at least 120 cells per n.

(G) Quantification of LD size frequencies fitted to a Gaussian distribution from micrographs in (E). At least 450 cells per genotype.

(H and I) Micrographs of WT and ΔΔ*ldo* cells expressing Nvj1^{GFP} and Vph1^{mScarlet} and corresponding quantification of NVJ size frequencies. 400–500 cells per genotype. Scale bars, 2 μm.

(J and K) Electron micrographs of ΔΔ*ldo* cells (32 h) showing piecemeal microautophagy of the nucleus (PMN) (J) and quantification of PMN vesicles (K). n = 56 (WT), n = 84 (ΔΔ*ldo*). Scale bars, 500 nm.

(L and M) Z projections of WT and ΔΔ*ldo* cells expressing Nvj1^{GFP} and Vph1^{mCherry} (L) and quantification of PMN vesicles (M). Data points and mean ± SEM; n = 3, at least 30 cells per n. Scale bars, 3 μm.

*p < 0.05, **p < 0.01, ***p < 0.001.

See related Figure S5 and Table S6 for statistical analyses.

Please cite this article in press as: Álvarez-Guerra et al., LDO proteins and Vac8 form a vacuole-lipid droplet contact site to enable starvation-induced lipophagy in yeast, Developmental Cell (2024), https://doi.org/10.1016/j.devcel.2024.01.014

exhaustion and is critical for efficient LD consumption via lipophagy.

The LDO proteins Ldo45 and Ldo16 were initially identified as accessory factors of yeast seipin, contributing to spatial organization of LD biogenesis at the ER.[36,37] Similar to the LDO proteins in yeast, also the lipid droplet assembly factor 1 (LDAF1 alias promethin), the putative mammalian LDO homolog, supports LD biogenesis by interacting with seipin and subsequently dissociates from seipin to target the surface of mature LDs.[60,61] We demonstrate that at a later step, when nutrients are exhausted, the LDO proteins establish vCLIP by redistributing to defined Vac8-positive foci of adjacent vacuoles. Similarly, also Pdr16, a cytosolic protein that is recruited to LDO-positive LDs,[36] redistributed to vCLIP in nutrient-exhausted cells. However, Pdr16 was not needed for either vCLIP formation or lipophagy. Interestingly, vCLIP formation occurs independently of several cellular processes and factors previously linked to lipophagy, including vacuolar microdomain formation, the ESCRT machinery and autophagy regulators.[31,33,34,45,46,62] Still, despite efficiently forming vCLIP, several of the analyzed mutants, in particular those defective in autophagy, displayed reduced vacuolar LD uptake, demonstrating that vCLIP formation is a prerequisite but not sufficient for successful lipophagy. Artificial docking of LDs to the vacuole in absence of LDO proteins did not restore lipophagy. Hence, mere contact formation does not trigger vacuolar uptake of LDs, suggesting that LDO proteins not only tether these organelles but in addition participate in the sequestration step.

Our data demonstrate that both LDO proteins are able to form vCLIP and to induce lipophagy, which contributes to long-term survival under caloric restriction. Their differential expression related to the cellular metabolic state likely reflects different roles in LD biology, and only Ldo16 is transcriptionally upregulated upon nutrient depletion. Our series of Ldo16 mutants revealed that its N-terminal hydrophobic domains insert it into the ER, its CAH redirects it to the LD surface, and its C-terminal intrinsically disordered peptide region directly binds Vac8 at the vacuolar surface. Formation of vCLIP and subsequent lipophagy was prevented by deleting *VAC8*, and phenocopied by loss of Pfa3, which palmitoylates Vac8 to anchor it to the vacuolar membrane. Notably, re-targeting Vac8 to the nuclear envelope was sufficient to re-route LDs to these sites, demonstrating that Vac8 is a vCLIP tether.

Multiple aspects of vacuolar homeostasis require the ARM repeat protein Vac8, which interacts with Atg13 and Atg11 to recruit the phagophore assembly site (PAS) to the vacuole to support bulk and selective autophagy, respectively, and interacts with Nvj1 to form the NVJ.[50,51,57,63] Crystallographic studies demonstrated that both Atg13 and Nvj1 interact with Vac8 via disordered loops that associate with the minor groove of the ARM repeat superhelix. According to ColabFold, the disordered loop of Ldo16 is predicted to occupy the same groove. Thus, Atg13, Nvj1 and Ldo16 might compete for binding, and Vac8 may switch from one binding partner to another to fine-tune multiple autophagic processes. Related to this, recruitment of the selective PAS to the vacuolar membrane has been proposed to derive from avidity-mediated Vac8-Atg11 interactions with low affinity that are stabilized by a high local concentration and limited diffusion of the interaction partners.[50,64] The same concept of a body to be autophagocytosed acting as a platform to concentrate Vac8 has been applied to the NVJ[55] and now can be seen in the context of LDs. Once an Ldo16-decorated LD comes into proximity with the rim of the NVJ, it can access a pool of highly concentrated Vac8, which exchanges its partner from Nvj1 to Ldo16 to form vCLIP. This concept places Vac8 as a key regulator of autophagic processes during starvation, with all of macroautophagy, PMN and lipophagy being routed through the same final common pathway. In support of this, we find that the loss of vCLIP formation upon genetic ablation of the LDO proteins results in NVJ expansion and induction of PMN. Vice versa, inactivation of NVJ formation triggers lipophagy. Though a functional link between PMN and lipophagy remains to be explored, our findings establish Vac8 as critical regulator of the contact sites that enable delivery of diverse cargo to the vacuole.

Limitations of the study

This study identifies the molecular tethering machinery critical to attach LDs to the vacuole for subsequent *en bloc* uptake, but knowledge gaps remain. How is the invagination of the vacuolar membrane at vCLIP achieved to push LDs inward and drive their uptake, and how do autophagy-related proteins contribute to this engulfment? In addition, the process of LD consumption inside the vacuolar lumen remains elusive. While our data suggest a slow and progressive consumption of LDs that supports long-term viability in stationary phase, how such gradual neutral lipid mobilization within the vacuole is mechanistically accomplished remains to be explored.

STAR★METHODS

Detailed methods are provided in the online version of this paper and include the following:

- KEY RESOURCES TABLE
- RESOURCE AVAILABILITY
  - Lead contact
  - Materials availability
  - Data and code availability
- EXPERIMENTAL MODEL AND STUDY PARTICIPANT DETAILS
  - Yeast strains and genetics
  - Yeast culturing conditions
- METHOD DETAILS
  - Analysis of cell growth
  - Flow cytometric analysis of cellular survival during aging
  - Immunoblot Analysis
  - Quantitative Real-Time PCR
  - Quantification of total cellular triacylglycerol levels
  - Confocal Fluorescence Microscopy
  - Image analysis and quantification
  - Transmission electron microscopy
  - Immuno-electron microscopy
  - Structural modelling
  - Vac8-Ldo16 interaction assay
  - Statistical analysis

SUPPLEMENTAL INFORMATION

Supplemental information can be found online at https://doi.org/10.1016/j.devcel.2024.01.014.

ACKNOWLEDGMENTS

This work was supported by Vetenskapsrådet (2019-05249 to S.B., 2019-04004 to J.L.H., 2019-04052 to C.A.), Knut and Alice Wallenberg Foundation (2017.009 to C.A., J.L.H., and S.B.), Stiftelsen Olle Engkvist Byggmästare (207-0527 to S.B.), Cancerfonden (20045 to C.A., 222488 to S.B., 211865 to J.L.H.) and Alfonso Martín Escudero foundation (to A.d.O.). We thank Christian Ungermann for the Vac8 antibody and Claudine Kraft for Vac8ΔN plasmids.

AUTHOR CONTRIBUTIONS

Conceptualization, I.Á.-G. and S.B.; methodology, I.Á.-G., E.B., F.B., S.G., T.I., A.d.O., L.H., C.A., T.P.L., J.L.H., and S.B.; investigation, I.Á.-G., E.B., F.B., S.G., T.I., A.d.O., L.H., and T.P.L.; formal analysis, I.Á.-G., F.B., and S.B.; resources, C.A., T.P.L., J.L.H., and S.B.; writing – original draft, I.Á.-G. and S.B.; writing – review & editing, T.P.L., C.A., and S.B.; supervision, C.A., T.P.L., J.L.H., and S.B.; funding acquisition, C.A., J.L.H., and S.B.

DECLARATION OF INTERESTS

The authors declare no competing interests.

Received: April 21, 2023
Revised: November 15, 2023
Accepted: January 18, 2024
Published: February 13, 2024

REFERENCES

1. Scorrano, L., De Matteis, M.A., Emr, S., Giordano, F., Hajnóczky, G., Kornmann, B., Lackner, L.L., Levine, T.P., Pellegrini, L., Reinisch, K., et al. (2019). Coming together to define membrane contact sites. Nat. Commun. *10*, 1287.
2. Eisenberg-Bord, M., Shai, N., Schuldiner, M., and Bohnert, M. (2016). A Tether Is a Tether Is a Tether: Tethering at Membrane Contact Sites. Dev. Cell *39*, 395–409.
3. Bohnert, M. (2020). Tether Me, Tether Me Not-Dynamic Organelle Contact Sites in Metabolic Rewiring. Dev. Cell *54*, 212–225.
4. Prinz, W.A., Toulmay, A., and Balla, T. (2020). The functional universe of membrane contact sites. Nat. Rev. Mol. Cell Biol. *21*, 7–24.
5. Phillips, M.J., and Voeltz, G.K. (2016). Structure and function of ER membrane contact sites with other organelles. Nat. Rev. Mol. Cell Biol. *17*, 69–82.
6. Kohler, V., and Büttner, S. (2021). Remodelling of Nucleus-Vacuole Junctions During Metabolic and Proteostatic Stress. Contact (Thousand Oaks) *4*, 25152564211016608.
7. Henne, W.M. (2016). Organelle remodeling at membrane contact sites. J. Struct. Biol. *196*, 15–19.
8. Kvam, E., and Goldfarb, D.S. (2007). Nucleus-vacuole junctions and piecemeal microautophagy of the nucleus in S. cerevisiae. Autophagy *3*, 85–92.
9. Tosal-Castano, S., Peselj, C., Kohler, V., Habernig, L., Berglund, L.L., Ebrahimi, M., Vögtle, F.-N., Höög, J., Andréasson, C., and Büttner, S. (2021). Snd3 controls nucleus-vacuole junctions in response to glucose signaling. Cell Rep. *34*, 108637.
10. Pan, X., Roberts, P., Chen, Y., Kvam, E., Shulga, N., Huang, K., Lemmon, S., and Goldfarb, D.S. (2000). Nucleus-vacuole junctions in *Saccharomyces cerevisiae* are formed through the direct interaction of Vac8p with Nvj1p. Mol. Biol. Cell *11*, 2445–2457.
11. Rogers, S., Hariri, H., Wood, N.E., Speer, N.O., and Henne, W.M. (2021). Glucose restriction drives spatial reorganization of mevalonate metabolism. eLife *10*, e62591.
12. Hariri, H., Rogers, S., Ugrankar, R., Liu, Y.L., Feathers, J.R., and Henne, W.M. (2018). Lipid droplet biogenesis is spatially coordinated at ER-vacuole contacts under nutritional stress. EMBO Rep. *19*, 57–72.
13. Barbosa, A.D., and Siniossoglou, S. (2016). Spatial distribution of lipid droplets during starvation: Implications for lipophagy. Commun. Integr. Biol. *9*, e1183854.
14. Olzmann, J.A., and Carvalho, P. (2019). Dynamics and functions of lipid droplets. Nat. Rev. Mol. Cell Biol. *20*, 137–155.
15. Walther, T.C., and Farese, R.V. (2012). Lipid droplets and cellular lipid metabolism. Annu. Rev. Biochem. *81*, 687–714.
16. Herker, E., Vieyres, G., Beller, M., Krahmer, N., and Bohnert, M. (2021). Lipid Droplet Contact Sites in Health and Disease. Trends Cell Biol. *31*, 345–358.
17. Liao, P.-C., Yang, E.J., Borgman, T., Boldogh, I.R., Sing, C.N., Swayne, T.C., and Pon, L.A. (2022). Touch and Go: Membrane Contact Sites Between Lipid Droplets and Other Organelles. Front. Cell Dev. Biol. *10*, 852021.
18. Thiam, A.R., and Dugail, I. (2019). Lipid droplet-membrane contact sites - from protein binding to function. J. Cell Sci. *132*, jcs230169.
19. Schuldiner, M., and Bohnert, M. (2017). A different kind of love - lipid droplet contact sites. Biochim. Biophys. Acta Mol. Cell Biol. Lipids *1862*, 1188–1196.
20. Shai, N., Yifrach, E., van Roermund, C.W.T., Cohen, N., Bibi, C., IJlst, L., Cavellini, L., Meurisse, J., Schuster, R., Zada, L., et al. (2018). Systematic mapping of contact sites reveals tethers and a function for the peroxisome-mitochondria contact. Nat. Commun. *9*, 1761.
21. Wang, J., Fang, N., Xiong, J., Du, Y., Cao, Y., and Ji, W.-K. (2021). An ESCRT-dependent step in fatty acid transfer from lipid droplets to mitochondria through VPS13D-TSG101 interactions. Nat. Commun. *12*, 1252.
22. Shin, D.W. (2020). Lipophagy: Molecular Mechanisms and Implications in Metabolic Disorders. Mol. Cells *43*, 686–693.
23. Singh, R., Kaushik, S., Wang, Y., Xiang, Y., Novak, I., Komatsu, M., Tanaka, K., Cuervo, A.M., and Czaja, M.J. (2009). Autophagy regulates lipid metabolism. Nature *458*, 1131–1135.
24. Grabner, G.F., Xie, H., Schweiger, M., and Zechner, R. (2021). Lipolysis: cellular mechanisms for lipid mobilization from fat stores. Nat. Metab. *3*, 1445–1465.
25. Graef, M. (2018). Lipid droplet-mediated lipid and protein homeostasis in budding yeast. FEBS Lett. *592*, 1291–1303.
26. Garcia, E.J., Vevea, J.D., and Pon, L.A. (2018). Lipid droplet autophagy during energy mobilization, lipid homeostasis and protein quality control. Front. Biosci. (Landmark Ed.) *23*, 1552–1563.
27. Zhang, X., Evans, T.D., Jeong, S.-J., and Razani, B. (2018). Classical and alternative roles for autophagy in lipid metabolism. Curr. Opin. Lipidol. *29*, 203–211.
28. Schulze, R.J., Krueger, E.W., Weller, S.G., Johnson, K.M., Casey, C.A., Schott, M.B., and McNiven, M.A. (2020). Direct lysosome-based autophagy of lipid droplets in hepatocytes. Proc. Natl. Acad. Sci. USA *117*, 32443–32452.
29. Schott, M.B., Rozeveld, C.N., Weller, S.G., and McNiven, M.A. (2022). Lipophagy at a glance. J. Cell Sci. *135*, jcs259402.
30. Seo, A.Y., Lau, P.-W., Feliciano, D., SenGupta, P., Gros, M.A.L., Cinquin, B., Larabell, C.A., and Lippincott-Schwartz, J. (2017). AMPK and vacuole-associated Atg14p orchestrate μ-lipophagy for energy production and long-term survival under glucose starvation. eLife *6*, e21690.
31. van Zutphen, T., Todde, V., de Boer, R., Kreim, M., Hofbauer, H.F., Wolinski, H., Veenhuis, M., van der Klei, I.J., and Kohlwein, S.D. (2014). Lipid droplet autophagy in the yeast *Saccharomyces cerevisiae*. Mol. Biol. Cell *25*, 290–301.

32. Vevea, J.D., Garcia, E.J., Chan, R.B., Zhou, B., Schultz, M., Di Paolo, G., McCaffery, J.M., and Pon, L.A. (2015). Role for Lipid Droplet Biogenesis and Microlipophagy in Adaptation to Lipid Imbalance in Yeast. Dev. Cell *35*, 584–599.

33. Liao, P.-C., Garcia, E.J., Tan, G., Tsang, C.A., and Pon, L.A. (2021). Roles for L o microdomains and ESCRT in ER stress-induced lipid droplet microautophagy in budding yeast. Mol. Biol. Cell *32*, br12.

34. Wang, C.-W., Miao, Y.-H., and Chang, Y.-S. (2014). A sterol-enriched vacuolar microdomain mediates stationary phase lipophagy in budding yeast. J. Cell Biol. *206*, 357–366.

35. Diep, D.T.V., Collado, J.F., Hugenroth, M., Wälte, M., Schmidt, O., Fernández-Busnadiego, R., and Bohnert, M. (2023). A metabolically controlled contact site between lipid droplets and vacuoles. https://doi.org/10.1101/2023.04.21.537652.

36. Eisenberg-Bord, M., Mari, M., Weill, U., Rosenfeld-Gur, E., Moldavski, O., Castro, I.G., Soni, K.G., Harpaz, N., Levine, T.P., Futerman, A.H., et al. (2018). Identification of seipin-linked factors that act as determinants of a lipid droplet subpopulation. J. Cell Biol. *217*, 269–282.

37. Teixeira, V., Johnsen, L., Martínez-Montañés, F., Grippa, A., Buxó, L., Idrissi, F.-Z., Ejsing, C.S., and Carvalho, P. (2018). Regulation of lipid droplets by metabolically controlled Ldo isoforms. J. Cell Biol. *217*, 127–138.

38. Müllner, H., Zweytick, D., Leber, R., Turnowsky, F., and Daum, G. (2004). Targeting of proteins involved in sterol biosynthesis to lipid particles of the yeast *Saccharomyces cerevisiae*. Biochim. Biophys. Acta *1663*, 9–13.

39. Exner, T., Beretta, C.A., Gao, Q., Afting, C., Romero-Brey, I., Bartenschlager, R., Fehring, L., Poppelreuther, M., and Füllekrug, J. (2019). Lipid droplet quantification based on iterative image processing. J. Lipid Res. *60*, 1333–1344.

40. Fontana, L., Partridge, L., and Longo, V.D. (2010). Extending healthy life span–from yeast to humans. Science *328*, 321–326.

41. Kory, N., Farese, R.V., and Walther, T.C. (2016). Targeting Fat: Mechanisms of Protein Localization to Lipid Droplets. Trends Cell Biol. *26*, 535–546.

42. Olarte, M.-J., Swanson, J.M.J., Walther, T.C., and Farese, R.V. (2022). The CYTOLD and ERTOLD pathways for lipid droplet-protein targeting. Trends Biochem. Sci. *47*, 39–51.

43. Pataki, C.I., Rodrigues, J., Zhang, L., Qian, J., Efron, B., Hastie, T., Elias, J.E., Levitt, M., and Kopito, R.R. (2018). Proteomic analysis of monolayer-integrated proteins on lipid droplets identifies amphipathic interfacial α-helical membrane anchors. Proc. Natl. Acad. Sci. USA *115*, E8172–E8180.

44. Prévost, C., Sharp, M.E., Kory, N., Lin, Q., Voth, G.A., Farese, R.V., and Walther, T.C. (2018). Mechanism and Determinants of Amphipathic Helix-Containing Protein Targeting to Lipid Droplets. Dev. Cell *44*, 73–86.e4.

45. Garcia, E.J., Liao, P.-C., Tan, G., Vevea, J.D., Sing, C.N., Tsang, C.A., McCaffery, J.M., Boldogh, I.R., and Pon, L.A. (2021). Membrane dynamics and protein targets of lipid droplet microautophagy during ER stress-induced proteostasis in the budding yeast, *Saccharomyces cerevisiae*. Autophagy *17*, 2363–2383.

46. Tsuji, T., Fujimoto, M., Tatematsu, T., Cheng, J., Orii, M., Takatori, S., and Fujimoto, T. (2017). Niemann-Pick type C proteins promote microautophagy by expanding raft-like membrane domains in the yeast vacuole. eLife *6*, e25960.

47. Henne, W.M., Zhu, L., Balogi, Z., Stefan, C., Pleiss, J.A., and Emr, S.D. (2015). Mdm1/Snx13 is a novel ER-endolysosomal interorganelle tethering protein. J. Cell Biol. *210*, 541–551.

48. Hou, H., Subramanian, K., LaGrassa, T.J., Markgraf, D., Dietrich, L.E.P., Urban, J., Decker, N., and Ungermann, C. (2005). The DHHC protein Pfa3 affects vacuole-associated palmitoylation of the fusion factor Vac8. Proc. Natl. Acad. Sci. USA *102*, 17366–17371.

49. Tang, F., Kauffman, E.J., Novak, J.L., Nau, J.J., Catlett, N.L., and Weisman, L.S. (2003). Regulated degradation of a class V myosin receptor directs movement of the yeast vacuole. Nature *422*, 87–92.

50. Hollenstein, D.M., Licheva, M., Konradi, N., Schweida, D., Mancilla, H., Mari, M., Reggiori, F., and Kraft, C. (2021). Spatial control of avidity regulates initiation and progression of selective autophagy. Nat. Commun. *12*, 7194.

51. Hollenstein, D.M., Gómez-Sánchez, R., Ciftci, A., Kriegenburg, F., Mari, M., Torggler, R., Licheva, M., Reggiori, F., and Kraft, C. (2019). Vac8 spatially confines autophagosome formation at the vacuole in S. cerevisiae. J. Cell Sci. *132*, jcs235002.

52. Hariri, H., Speer, N., Bowerman, J., Rogers, S., Fu, G., Reetz, E., Datta, S., Feathers, J.R., Ugrankar, R., Nicastro, D., et al. (2019). Mdm1 maintains endoplasmic reticulum homeostasis by spatially regulating lipid droplet biogenesis. J. Cell Biol. *218*, 1319–1334.

53. Pan, X., and Goldfarb, D.S. (1998). YEB3/VAC8 encodes a myristylated armadillo protein of the *Saccharomyces cerevisiae* vacuolar membrane that functions in vacuole fusion and inheritance. J. Cell Sci. *111*, 2137–2147.

54. Jeong, H., Park, J., Kim, H.-I., Lee, M., Ko, Y.-J., Lee, S., Jun, Y., and Lee, C. (2017). Mechanistic insight into the nucleus-vacuole junction based on the Vac8p-Nvj1p crystal structure. Proc. Natl. Acad. Sci. USA *114*, E4539–E4548.

55. Park, J., Kim, H.-I., Jeong, H., Lee, M., Jang, S.H., Yoon, S.Y., Kim, H., Park, Z.-Y., Jun, Y., and Lee, C. (2020). Quaternary structures of Vac8 differentially regulate the Cvt and PMN pathways. Autophagy *16*, 991–1006.

56. Mirdita, M., Schütze, K., Moriwaki, Y., Heo, L., Ovchinnikov, S., and Steinegger, M. (2022). ColabFold: making protein folding accessible to all. Nat. Methods *19*, 679–682.

57. Roberts, P., Moshitch-Moshkovitz, S., Kvam, E., O'Toole, E., Winey, M., and Goldfarb, D.S. (2003). Piecemeal microautophagy of nucleus in *Saccharomyces cerevisiae*. Mol. Biol. Cell *14*, 129–141.

58. Kounakis, K., Chaniotakis, M., Markaki, M., and Tavernarakis, N. (2019). Emerging Roles of Lipophagy in Health and Disease. Front. Cell Dev. Biol. *7*, 185.

59. Pressly, J.D., Gurumani, M.Z., Varona Santos, J.T., Fornoni, A., Merscher, S., and Al-Ali, H. (2022). Adaptive and maladaptive roles of lipid droplets in health and disease. Am. J. Physiol. Cell Physiol. *322*, C468–C481.

60. Castro, I.G., Eisenberg-Bord, M., Persiani, E., Rochford, J.J., Schuldiner, M., and Bohnert, M. (2019). Promethin Is a Conserved Seipin Partner Protein. Cells *8*, 268.

61. Chung, J., Wu, X., Lambert, T.J., Lai, Z.W., Walther, T.C., and Farese, R.V. (2019). LDAF1 and Seipin Form a Lipid Droplet Assembly Complex. Dev. Cell *51*, 551–563.e7.

62. Oku, M., Maeda, Y., Kagohashi, Y., Kondo, T., Yamada, M., Fujimoto, T., and Sakai, Y. (2017). Evidence for ESCRT- and clathrin-dependent microautophagy. J. Cell Biol. *216*, 3263–3274.

63. Gatica, D., Wen, X., Cheong, H., and Klionsky, D.J. (2021). Vac8 determines phagophore assembly site vacuolar localization during nitrogen starvation-induced autophagy. Autophagy *17*, 1636–1648.

64. Erlendsson, S., and Teilum, K. (2020). Binding Revisited-Avidity in Cellular Function and Signaling. Front. Mol. Biosci. *7*, 615565.

65. Pfirrmann, T., Heessen, S., Omnus, D.J., Andréasson, C., and Ljungdahl, P.O. (2010). The prodomain of Ssy5 protease controls receptor-activated proteolysis of transcription factor Stp1. Mol. Cell. Biol. *30*, 3299–3309.

66. Schindelin, J., Arganda-Carreras, I., Frise, E., Kaynig, V., Longair, M., Pietzsch, T., Preibisch, S., Rueden, C., Saalfeld, S., Schmid, B., et al. (2012). Fiji: an open-source platform for biological-image analysis. Nat. Methods *9*, 676–682.

67. Janke, C., Magiera, M.M., Rathfelder, N., Taxis, C., Reber, S., Maekawa, H., Moreno-Borchart, A., Doenges, G., Schwob, E., Schiebel, E., et al. (2004). A versatile toolbox for PCR-based tagging of yeast genes: new fluorescent proteins, more markers and promoter substitution cassettes. Yeast *21*, 947–962.

68. Heckman, K.L., and Pease, L.R. (2007). Gene splicing and mutagenesis by PCR-driven overlap extension. Nat. Protoc. *2*, 924–932.

69. Storici, F., and Resnick, M.A. (2006). The Delitto Perfetto Approach to In Vivo Site-Directed Mutagenesis and Chromosome Rearrangements with Synthetic Oligonucleotides in Yeast. In Methods in Enzymology DNA Repair, Part B. (Academic Press), pp. 329–345.

70. Holmberg, M.A., Gowda, N.K.C., and Andréasson, C. (2014). A versatile bacterial expression vector designed for single-step cloning of multiple DNA fragments using homologous recombination. Protein Expr. Purif. *98*, 38–45.

71. Ebrahimi, M., Habernig, L., Broeskamp, F., Aufschnaiter, A., Diessl, J., Atienza, I., Matz, S., Ruiz, F.A., and Büttner, S. (2021). Phosphate Restriction Promotes Longevity via Activation of Autophagy and the Multivesicular Body Pathway. Cells *10*, 3161.

72. Peselj, C., Ebrahimi, M., Broeskamp, F., Prokisch, S., Habernig, L., Alvarez-Guerra, I., Kohler, V., Vögtle, F.-N., and Büttner, S. (2022). Sterol Metabolism Differentially Contributes to Maintenance and Exit of Quiescence. Front. Cell Dev. Biol. *10*, 788472.

73. Diessl, J., Berndtsson, J., Broeskamp, F., Habernig, L., Kohler, V., Vazquez-Calvo, C., Nandy, A., Peselj, C., Drobysheva, S., Pelosi, L., et al. (2022). Manganese-driven CoQ deficiency. Nat. Commun. *13*, 6061.

74. Livak, K.J., and Schmittgen, T.D. (2001). Analysis of Relative Gene Expression Data Using Real-Time Quantitative PCR and the 2-ΔΔCT Method. Methods *25*, 402–408.

75. Bunk, D., Moriasy, J., Thoma, F., Jakubke, C., Osman, C., and Hörl, D. (2022). YeastMate: neural network-assisted segmentation of mating and budding events in *Saccharomyces cerevisiae*. Bioinformatics *38*, 2667–2669.

76. Stringer, C., Wang, T., Michaelos, M., and Pachitariu, M. (2021). Cellpose: a generalist algorithm for cellular segmentation. Nat. Methods *18*, 100–106.

77. Hawes, P., Netherton, C.L., Mueller, M., Wileman, T., and Monaghan, P. (2007). Rapid freeze-substitution preserves membranes in high-pressure frozen tissue culture cells. J. Microsc. *226*, 182–189.

78. Reynolds, E.S. (1963). The use of lead citrate at high pH as an electron-opaque stain in electron microscopy. J. Cell Biol. *17*, 208–212.

79. Panagaki, D., Croft, J.T., Keuenhof, K., Larsson Berglund, L., Andersson, S., Kohler, V., Büttner, S., Tamás, M.J., Nyström, T., Neutze, R., et al. (2021). Nuclear envelope budding is a response to cellular stress. Proc. Natl. Acad. Sci. USA *118*, e2020997118.

80. Kremer, J.R., Mastronarde, D.N., and McIntosh, J.R. (1996). Computer visualization of three-dimensional image data using IMOD. J. Struct. Biol. *116*, 71–76.

81. Ashkenazy, H., Erez, E., Martz, E., Pupko, T., and Ben-Tal, N. (2010). ConSurf 2010: calculating evolutionary conservation in sequence and structure of proteins and nucleic acids. Nucleic Acids Res. *38*, W529–W533.

Please cite this article in press as: Álvarez-Guerra et al., LDO proteins and Vac8 form a vacuole-lipid droplet contact site to enable starvation-induced lipophagy in yeast, Developmental Cell (2024), https://doi.org/10.1016/j.devcel.2024.01.014

STAR★METHODS

KEY RESOURCES TABLE

REAGENT or RESOURCE	SOURCE	IDENTIFIER
Antibodies		
Goat polyclonal anti-Rabbit IgG (whole molecule) - Peroxidase	SIGMA-ALDRICH	Cat#A0545; RRID: AB_257896
Mouse monoclonal anti-GFP	SIGMA-ALDRICH	Cat#1814460001; RRID: AB_390913
Mouse monoclonal anti-GAPDH	Thermo Fischer	Cat # MA5-15738; RRID: AB_10977387
Rabbit polyclonal anti-Mouse IgG (whole molecule) - Peroxidase	SIGMA-ALDRICH	Cat#A9044; RRID: AB_258431
Goat anti-Rabbit IgG (H&L), 10 nm gold	EMS Electron Microscopy Sciences	Cat#25108
Rabbit monoclonal anti-Tubulin	Abcam	Cat#ab184970; RRID: AB_2819060
Rabbit anti-Vac8	Gift from Christian Ungermann	N/A
Rabbit anti-GST	Pfirrmann et al.[65]	N/A
Rabbit anti-Sumo	Affinity-purified antibody from serum	N/A
Chemicals, Peptides, and Recombinant Proteins		
CellTracker Blue CMAC	Thermo Fisher	Cat#C2110
Clarity Western ECL Substrate	BIO-RAD	Cat#1705060
Tween-20	SIGMA-ALDRICH	Cat#P5927
Formvar	TAAB	Cat#F004
KAPA SYBR Fast qPCR Master mix (2x)	SIGMA ALDRICH	Cat#KK4600
Lowicryl HM20	Polysciences	Cat#15924-1
Sodium oleate	SIGMA ALDRICH	Cat#O3880
Invitrogen Bodipy 493/503	Fischer Scientific	Cat#11540326
Invitrogen FM4-64FX	Fischer Scientific	Cat#11574816
Monodansylpentane (MDH)	Abcepta	Cat#SM1000b
SuperScript II Reverse Transcriptase	Thermo Fisher	Cat#18064014
TURBO DNase	Thermo Fisher	Cat#AM2239
Propidium iodide	SIGMA-ALDRICH	Cat#81845-100MG
IGEPAL CA-630	SIGMA-ALDRICH	Cat# I8896-100ML
Protino Glutathione Agarose 4B beads	MACHEREY-NAGEL GmbH&Co- KG	Cat#745500.10
Critical Commercial Assays		
RiboPure RNA Purification Kit	Thermo Fisher	Cat#AM1926
Triglyceride Assay Kit	Abcam	Cat#ab65336
Experimental Models: Organisms/Strains		
All yeast strains used in this study are listed in Table S1		
Oligonucleotides		
All oligonucleotides used in this study are listed in Table S3 (for gene deletion), Table S4 (for gene tagging), and Table S5 (for gene truncation and mutation).		
Plasmids used in this study		
All plasmids used in this study are listed in Table S2		
Software and Algorithms		
Adobe illustrator CC 22.0.1	Adobe	RRID:SCR_010279
Affinity designer v1	Serif (Europe) Ltd.	RRID:SCR_016952
Fiji	Schindelin et al.[66]	RRID: SCR_002285
Image Lab 5.2.1 Software	BIO-RAD	Cat#1709690
IMOD	the Regents of the University of Colorado	RRID: SCR_003297
Graphpad PRISM (8.0)	GraphPad Software	RRID:SCR_002798

(*Continued on next page*)

Please cite this article in press as: Álvarez-Guerra et al., LDO proteins and Vac8 form a vacuole-lipid droplet contact site to enable starvation-induced lipophagy in yeast, Developmental Cell (2024), https://doi.org/10.1016/j.devcel.2024.01.014

Continued

REAGENT or RESOURCE	SOURCE	IDENTIFIER
ZEN blue software control	ZEISS	RRID:SCR_013672
Black ZEN software	ZEISS	RRID:SCR_018163
guavaSoft 3.3 software	Luminex Corporate	N/A
Others		
Ceta CMOS 16M camera	FEI Co.	N/A
ChemiDoc XRS+ Imaging System	BIO-RAD	Cat#1708265
2300 EnSpire	PerkinElmer	N/A
Guava easyCyte HT	Luminex Corporate	N/A
LSM780	ZEISS	N/A
LSM800	ZEISS	N/A
Plan-Apochromat 63x/1.40 Oil M27 objective	ZEISS	N/A
Reichert-Jung Ultracut E Ultramicrotome	C. Reichert	N/A
Roti-PVDF, pore size 0.45 μm	ROTH	Cat#T830.1
Tecnai T12 electron microscope	FEI Co.	N/A
Ultra 45° diamond knife	Diatome	N/A
96 Well Microplate, clear, flat bottom	Greiner BIO-ONE	Cat#655101
Wohlwend Compact 03	M. Wohlwend GmbH	N/A
Oakton Glass Beads for Mills	Thermo Fisher	Cat#12614267
Bioprep-24-Homogenizer	Allsheng	Cat#AS-13010-00
Emulsiflex-B15 homogenizer	Avestin	N/A

RESOURCE AVAILABILITY

Lead contact

Further information and requests for resources and reagents should be directed to and will be fulfilled by the lead contact, Sabrina Büttner (sabrina.buettner@su.se).

Materials availability

All materials generated in this study will be available from the lead contact.

Data and code availability

This study did not generate any unique datasets or code.

EXPERIMENTAL MODEL AND STUDY PARTICIPANT DETAILS

Yeast strains and genetics

All experiments were performed in BY4742 (*MATα*; *his3*Δ1; *leu2*Δ0; *lys2*Δ0; *ura3*Δ0) or BY4741 (*MATa his3*Δ1; *leu2*Δ0; *met15*Δ0; *ura3*Δ0). Yeast transformations were conducted as previously described, and deletion or endogenous tagging of genes via homologous recombination was performed following standard procedure.[67] All yeast strains and plasmids used in this study are listed in Tables S1 and S2, respectively. Oligonucleotides used in this study are listed in Table S3 (for gene deletion), in Table S4 (for gene tagging), and in Table S5 (for gene truncation and mutation). The plasmids encoding Ldo45 or GFP-tagged Ldo45 (pRS313-spLdo45 and pRS313-spLdo45^{GFP}, respectively) were created by PCR amplification of respective fragments from the genome, excluding the intron region and including the Ldo45 promoter, followed by fragment joining by overlapping PCR.[68] For pRS313-spLdo45^{GFP}, a yeGFP from pYM25 was C-terminally added. The final constructs were introduced into the pRS313 backbone using *BamH*I and *Xho*I restriction sites. The pRS313-Ldo16 and pRS313-Ldo16^{GFP} plasmids were constructed in the same way, amplifying the genomic *YMR148w* region. Truncation mutants of Ldo16 and Ldo45 (Ldo16$^{\Delta C24}$, Ldo16$^{\Delta C54}$, Ldo16$^{\Delta C94}$, Ldo16$^{\Delta N49}$, Ldo16$^{\Delta N72}$, Ldo45$^{\Delta C148}$) were created by amplifying the corresponding fragments from the pRS313-spLdo45^{GFP} or the pRS313-Ldo16^{GFP} plasmid and fusing them by overlapping PCR, preserving the promoter, the yeGFP sequence and the plasmid backbone. To create the Ldo16 variants carrying point mutations in the putative cationic amphipathic helix (pRS313-Ldo16^{5xA} and pRS313-Ldo16^{2xE}) the point mutations were introduced in respective oligonucleotides, and the amplified fragments containing the mutated sites were joined with overlapping PCR. The genomic single deletion of *LDO16* (Δ*ldo16*) was created using the *delitto perfetto* approach.[69] Briefly, the open reading frame coding for Ldo45 and Ldo16 was first substituted with a cassette containing *KlURA3* and *kanMX4*.

Please cite this article in press as: Álvarez-Guerra et al., LDO proteins and Vac8 form a vacuole-lipid droplet contact site to enable starvation-induced lipophagy in yeast, Developmental Cell (2024), https://doi.org/10.1016/j.devcel.2024.01.014

Then, the sequence corresponding to spliced *LDO45* was amplified from pRS313-spLdo45 and recombined to replace the cassette. For plasmid construction for the Vac8-Ldo16 interaction assay in *E. coli*, a 2.9 kb DNA fragment was synthesized, encompassing codon-optimized Ldo16$_{50-148}$-RBS-GST-Vac8 with sequences homologous to pSUMO-YHRC. Following yeast homologous recombination with pSUMO-YHRC as previously described,[70] pCA1057 (coding for Sumo-Ldo16$_{50-148}$-RBS-GST-Vac8) was isolated as a kanamycin-resistant clone. The derivative pCA1056 (coding for Sumo-Ldo16$_{50-148}$-RBS-GST) was constructed by *Hind*III restriction of pCA1057 to release *VAC8* sequences followed by religation.

Yeast culturing conditions

All strains were grown in baffled Erlenmeyer flasks at 28°C and shaking at 145 rpm in synthetic complete medium (SC), containing 0.17% yeast nitrogen base (BD Difco), 0.5% $(NH_4)_2SO_4$ (Carl Roth) and 30 mg/l of all amino acids (except 80 mg/l histidine and 200 mg/l leucine and, for the BY4742 strain, 120 mg/l lysine), 30 mg/l adenine and 320 mg/l uracil, with 2% glucose (SCD) or 0.4% glucose (SCD 0.4%) for caloric restriction. Plasmid-containing strains were grown in SCD without histidine, uracil or leucine. Overnight cultures were incubated for 16-20 h in SCD and used to inoculate cultures to OD_{600} 0.1 in SCD, followed by culturing into glucose exhaustion and stationary phase. For caloric restriction, overnight cultures in SCD were used to inoculate cells to OD_{600} 0.1 in SCD 0.4%, followed by culturing and rapid exhaustion of the limited glucose. For nitrogen starvation conditions, cells were pre-inoculated at 0.01 OD_{600} and grown in SCD for 12 h, washed with water and diluted 1:10 into SD without $(NH_4)_2SO_4$ and amino acids (SD-N). For phosphate restriction, cells were inoculated in SCD prepared using YNB without phosphate (FORMEDIUM). Phosphate was supplemented as NaH_2PO_4 to a final concentration of 0.2 mM (instead of 7 mM as in standard SCD), allowing regular growth but leading to early entry into stationary phase due to phosphate exhaustion as described before.[71,72] For oleate supplementation, cultures were inoculated to OD_{600} 0.1 in SCD and grown for 5 h before addition of 0.5% sodium oleate (final concentration; dissolved in 0.1% Tween-20) (Sigma-Aldrich O3880) or of the respective solvent control. For deletion and tagging of genes, yeast cells were grown in rich medium (YPD) containing 20 g/l peptone (Gibco Bacto BD Biosciences), 10 g/l yeast extract (Bacto BD Biosciences) and 4% glucose. For subsequent selection of mutants, YPD plates containing hygromycin B (FORMEDIUM, HYG5000), nourseothricin sulphate (Jena Biosciences, AB102XL) or G418 (Sigma-Aldrich, A1720-5G) or SCD plates with all amino acids except for histidine, uracil or leucine, were used.

METHOD DETAILS

Analysis of cell growth

Cells from overnight cultures were used to inoculate 250 μl SCD to OD_{600} 0.1 in 96-well microplates with clear, flat bottom (Greiner Bio-ONE). Plates were shaking at 999 rpm and 28°C and growth was measured by monitoring OD_{600} every 2 h for 10 h using a plate reader (2300 EnSpire, Perkin Elmer).

Flow cytometric analysis of cellular survival during aging

Cellular survival was determined using propidium iodide (PI) staining, indicative of loss of plasma membrane integrity and thus cell death.[73] Cultures were inoculated in standard glucose media with 2% glucose (SCD) or caloric-restricted media (SCD 0.4%) as described above, and aliquots were collected at indicated days during chronological aging. Cells were transferred into 96-well plates, pelleted by centrifugation at 3500 rpm for 1 min and resuspended in 250 μl PBS containing PI (Sigma-Aldrich, 81845) with a final concentration of 0.02 μg/ml (early days) or 0.1 μg/ml (late days), followed by incubation in the dark for 10 min. Cells were pelleted, resuspended in PBS and evaluated via flow cytometry using a Guava easyCyte HT with guavaSoft 3.3 software (Luminex Corporate). 5000 cells were analyzed per sample, and PI negative cells were scored as alive.

Immunoblot Analysis

6 OD_{600} of cells were harvested by centrifugation, lysed with lysis buffer (1.85 M NaOH; 7.5% β-mercaptoethanol) and incubated on ice for 10 min. After addition of 55% TCA, samples were again incubated on ice for 10 min, centrifugated for 10 min at 4°C, and the pellets were resuspended in urea loading buffer (200 mM Tris-HCl; 8 M urea; 5% SDS; 1 mM EDTA; 0.02% bromophenol blue; 15 mM DTT; pH 6.8). Samples were incubated for 10 min at 65°C, centrifuged and the supernatant was loaded on 12.5% polyacrylamide gels for separation via SDS-PAGE, followed by blotting on PVDF membranes (ROTH). Membranes were blocked in 5% milk/TBS (500 mM Tris; 1.5 M NaCl; pH 7.4) and were fixed by incubating them shaking in acetone for 30 min at 4°C. Then membranes were dried at 50°C for another 30 min, reactivated with 99% ethanol, washed and probed with antibodies against the GFP-epitope (dilution 1:2500, mouse, Roche 181446001), α-Tubulin (dilution 1:10000, rabbit, Abcam, 184970), GAPDH (dilution 1:10000, mouse, Thermo Fischer, MA5-15738), GST (dilution 1:5000, purified rabbit polyclonal antibody[65]), Sumo (dilution 1:5000, rabbit, Smt3-affinity purified antibody from serum), and Vac8 (dilution 1:10000, rabbit, gift from Christian Ungermann) as well as respective peroxidase-conjugated secondary antibodies against mouse (dilution 1:10000, rabbit, Sigma A9044) or rabbit (dilution 1:10000, goat, Sigma A0545). Clarity Western ECL Substrate (BIO-RAD) and a ChemiDoc XRS + Imaging System (BIO-RAD) were used for detection. Densitometric quantification was performed with Image Lab 5.2.1 Software (BIO-RAD).

Quantitative Real-Time PCR

To assess gene expression via qRT-PCR, approximately 30 OD_{600} of cells were collected and total RNA was purified using the Ribopure-Yeast kit (Thermo Fisher, AM1926). Genomic DNA was digested using TURBO DNase (Invitrogen AM2238) according

to the supplier's protocol. 2 μg of total RNA was reverse transcribed with SuperScript transcriptase (Thermo Fisher, 18064014) following the manufacturer's instructions. qRT-PCR was performed in triplicates with the KAPA SYBR Fast qPCR Master mix (Sigma-Aldrich, KK4600) using a Rotor-Gene Q (Qiagen) PCR cycler. Data are presented as fold changes using the comparative Ct method (ΔΔCT)[74] and *UBC6* as housekeeping gene. All primers used for qRT-PCR are listed in Table S5.

Quantification of total cellular triacylglycerol levels

10 OD_{600} of cells, cultured for 48 h in SCD, were harvested, washed with cold PBS and resuspended in 5% IGEPAL CA-630 (Sigma-Aldrich, I8896). Cells were mixed with glass beads and lysed with a Bioprep-24 homogenizer (Allsheng), using 3 cycles of 30 s. Similar volumes of the resulting lysates, corresponding to similar amounts of cells, were used to measure triacylglycerol levels using the Triglyceride Assay Kit (Abcam, ab65336) according to the manufacturer's instructions. To account for background signal due to the presence of diacylglycerol and in particular glycerol in the samples, each sample was corrected by a background control of its own without addition of lipase. Thus, the values obtained without lipase addition were subtracted from the values obtained for the same sample upon addition of lipase. Cells lacking the two acyltransferases Dga1 and Lro1 and hence almost completely devoid of triacylglycerols were used as negative controls, resulting in values resembling background. Measurements were obtained by recording fluorescence intensity (excitation at 535 nm; emission at 570 nm) with a plate reader (2300 EnSpire, Perkin Elmer).

Confocal Fluorescence Microscopy

1 OD_{600} of cells were harvested at indicated time points, stained using indicated dyes as described below and seeded on 3% agar/PBS (137 mM NaCl, 2.7 mM KCl, 10 mM Na_2HPO_4, 1.8mM KH_2PO_4; pH 7.4). The samples were imaged using a ZEISS LSM780 microscope equipped with an 63x/1.40 Oil M27 objective using the ZEN black software. For Figures 1G, 4H, and S3B, a ZEISS LSM800 Airyscan microscope equipped with an 63x/1.40 Oil M27 objective and the ZEN blue software control was used. Appropriate laser and detector settings were applied to visualize endogenously tagged proteins (GFP, mCherry or mScarlet) or dyes. For LD stainings, wells were incubated for 10 min in the dark with BODIPY493/503 (0.12 nM; Fischer Scientific, 11540326) or monodansylpentane (MDH) (100 μM; AUTODOT Abcepta, #SM1000b) and then washed with PBS prior to seeding on agar-coated slides and microscopic analysis. For vacuolar staining, cells were either incubated for 30 min in the dark with CellTracker Blue 7-amino-4-chloromethylcoumarin (CMAC) Dye (1 mM; Thermo Fisher, C2111) and washed with PBS before imaging, or supplemented with FM 4-64FX (Invitrogen, 11574816) to a final concentration of 15 μM directly in the culture media until collecting the cells for microscopic analysis.

Image analysis and quantification

Images obtained with the ZEISS LSM800 Airyscan were first processed using the "Airyscan processing" algorithm in the ZEN blue software. The open-source software Fiji[66] was used to further process and quantify all confocal micrographs. To process the images, Gaussian filtering (s = 0.8-1.5) was applied, followed by background subtraction (rolling ball radius = 25–50 pixels) and Unsharp mask settings when required. Images from the same experiment were processed with similar settings. Brightness and contrast were adjusted for each channel equally in individual experiments for analysis. The ratio of 'LDs in/out' of the vacuole using BODIPY was calculated by automatically measuring Integrated Density (IntDen) 'inside of vacuoles' segmented with the Huang algorithm and divided by the IntDen of 'outside of vacuoles' (calculated by subtracting the IntDen 'inside the vacuoles' from the IntDen of the whole cell, segmented with YeastMate or Cellpose 2[75,76]). 'Relative lipophagy' was obtained by calculating the 'LDs in/out' ratio of MDH-stained cells and normalizing by the control averaged ratio. All intensity measurements were performed in the original, unprocessed images. LD size was quantified by segmenting LDs with the Yen algorithm and measurement of the area. Number of LDs per cell was quantified by automated counting of the segmented LDs against the mask of segmented cells with Find Maxima. In both cases, the results were analyzed with a frequency distribution and were fitted to a gaussian curve. The colocalization analysis to obtain the Pearson's and Manders M2 coefficients was performed with the JaCoP plugin, thresholding images with only Gaussian blur, subtract background and Unsharp Mask adjusted. Quantification of cells according to LDO^{GFP} distribution (Figure 5E) as well as according to NVJ formation using $Nvj1^{GFP}$ (Figure 5F) in the Vac8 truncation mutants was performed manually using the Cell counter plugin.

Transmission electron microscopy

For transmission electron microscopy, samples were prepared as described.[9] Briefly, a Wohlwend Compact 03 (M. Wohlwend GmbH, Sennwald, Switzerland) was used for high-pressure freezing of samples, and freeze-substitution was performed for 1 h in a Leica EM AFS2 (Leica Microsystems, Vienna, Austria) using the Leica reagent bath with a flow-through ring of 2% uranyl acetate dissolved in 90% acetone and 10% methanol at -90°C.[77] Samples were washed twice in acetone while the temperature was gradually raised (2.9°C per h to -50°C). Samples were infiltrated with increasing amounts of Lowicryl HM20 (Polysciences, Warrington, PA, 15924-1) mixed with acetone (1:4, 2:3, 1:1, 4:1 and 100% 3x) at -50°C and a duration of 2 h per step. UV light was used to induce polymerization for 72 h at -50°C, followed by 24 h at room temperature. A Reichert-Jung Ultracut E Ultramicrotome (C. Reichert, Vienna, Austria) with an ultra 45° diamond knife (Diatome, Biel, Switzerland) was used to cut sections of 70 nm, which were collected on copper slot grids coated with 1% Formvar (TAAB). 2% uranyl acetate in dH_2O and Reynold's lead citrate were applied for on-section contrast staining.[78] A Tecnai T12 electron microscope equipped with a Ceta CMOS 16M camera (FEI Co., Eindhoven, the Netherlands) was used for imaging of samples at 120 kV. Quantification of LDs in direct physical contact with the vacuole or the ER as well as PMN events per section was performed manually.

Please cite this article in press as: Álvarez-Guerra et al., LDO proteins and Vac8 form a vacuole-lipid droplet contact site to enable starvation-induced lipophagy in yeast, Developmental Cell (2024), https://doi.org/10.1016/j.devcel.2024.01.014

Immuno-electron microscopy

For immunogold labelling, the sample blocks were prepared and embedded in HM20 resin as described above, as this sample preparation has been shown to be amenable to immune-labelling.[79] Grids with 70 nm-thick sections were fixed in 1% paraformaldehyde in PBS for 10 min and blocked with 0.1% fish skin gelatin and 0.8% BSA in PBS for 1 h. For primary antibody labeling, samples were incubated overnight with an antibody against Vac8 (dilution 1:30, rabbit, gift from Christian Ungermann), followed by 3x wash in PBS for 20 min and 1 h incubation with a secondary gold-conjugated antibody (anti-rabbit IgG 10 nm gold; EMS Electron Microscopy Sciences). After washing with PBS, glutaraldehyde (2.5%) was applied to the sections for postfixing for 1 h, followed by contrast staining using uranyl acetate and Reynold's lead citrate as described above. The detection of gold particles was done automatically using the IMODfindbeads program[80] inside of an area including 30 nm (the size of the antibody sandwich plus the gold particle) on either side of the membranes. Special drawing tools were used to efficiently model such areas in the IMOD suite of programs, followed by automated extraction of the quantification of the gold beads per area. Vac8 labeling density was quantified at vacuolar membrane regions in contact with LDs (vCLIP), in contact with the nER (NVJs), not in contact with other organelles (vacuolar membrane) and at the nER excluding the NVJs. In total, 57 sections were quantified, with varying numbers of data points for the 4 membrane categories, depending on their presence in respective section.

Structural modelling

To model the conservation of the Vac8 surface, a multiple sequence alignment was made that focussed on Vac8 only using 2 rounds of HHblits, which searches into a nr30 database (non-redundant above 30% identity). After the first iteration 106 hits were included with e-value $<10^{-20}$. After the second iteration, 294 proteins were included (e-value $< 10^{-42}$). This excluded other Armadillo repeat proteins. Aligned sequences were submitted along with the solved structure of Vac8 to the ConSurf server[81] to obtain conservation scores for residues on the surface scaled between 0-10. To model the interaction of Vac8 with Ldo16, ColabFold[56] was seeded with Vac8 residues (560 residues, 19-578, missing the disordered N-terminus) and full length Ldo16 (148 residues). The structure shown in Figure 5H is the rank 1 model, for which a version was obtained with side-chains positioned in relaxed conformations.

Vac8-Ldo16 interaction assay

E. coli BL21(DE3) cells were transformed with pCA1056 and pCA1057 that co-express Sumo- Ldo16$^{\Delta N49}$ with GST or GST-Vac8, respectively. Cells were grown in salt free 2xYT (1.6% tryptone and 1% yeast extract) supplemented with 50 mg/L kanamycin and 2 mM $MgSO_4$ at 30°C until OD_{600} reached 0.8-1. Protein expression was induced by the addition of 0.5 mM IPTG and 300 mM NaCl. The cells were harvested after 4 h and were resuspended in LWB150 lysis buffer (40 mM Hepes-KOH pH 7.4, 150 mM KCl, 5 mM $MgCl_2$, 5% (v/v) glycerol, 1 mM PMSF, 10 mM β-mercaptoethanol) and lysed by three passages through a Emulsiflex-B15 homogenizer (Avestin). The lysates were centrifuged at 19 000 g for 30 min at 4°C and the supernatants were incubated with Protino Glutathione Agarose 4B beads (MACHEREY-NAGEL GmbH & Co. KG) for 2 h at 4°C. The beads were washed thrice with LWB150 buffer and eluted with the same buffer containing 10 mM reduced glutathione. The proteins levels were analyzed by SDS-PAGE and immunoblotting.

Statistical analysis

Data are presented either as dot plots, showing individual data points, mean (line) and error bars representing standard error of mean (SEM), or as line graphs with symbols depicting mean and SEM (survival as well as protein and mRNA level) or as line graphs depicting a gaussian non-linear regression fit histogram (frequency distribution). Sample size, referring to independent biological replicates, is indicated in the respective figure legends. Statistical analysis was performed using GraphPad Prism (v8.0). Shapiro-Wilk's test and visual inspection of Q-Q-plots was used to check for normal distribution of data, and analysis of variance (ANOVA) with Tukey's *post hoc* test was used for comparisons between multiple groups. The equality of group variances was checked with the Brown-Forsythe-Test. Due to unequal variances of data shown in Figures 2F and 6B, a *Welch's t* Test or a *Welch's* ANOVA with *Dunnett T3 post hoc* test was used. Where appropriate, a two-way ANOVA, corrected with *Tukey's* or *Bonferroni's multiple comparisons test*, was applied. Significances are presented as ***p<0.001, **p<0.01, and *p<0.05. Details for all statistical analyses performed are listed in Table S6.